Research Article

Study on Dynamic Amplification Coefficient of U-Shaped Girder Based on Vehicle-Bridge Coupling Dynamics

Tangying Bai [ID],[1] **Hui Li** [ID],[2] **Yu Tian** [ID],[1] **Yipeng Chen** [ID],[1] **Yudong Wen** [ID],[3] **and Chaoyi Xia** [ID][3]

[1]*Beijing Urban Construction Design & Development Group Co., Ltd., Beijing 100037, China*
[2]*Nanjing Metro Construction Co., Ltd., Nanjing 210037, China*
[3]*Beijing Jiaotong University, Beijing 100044, China*

Correspondence should be addressed to Chaoyi Xia; xiacy88@163.com

In this paper, a vehicle-bridge coupling dynamic model is established considering the vertical wheel-rail tight contact and the lateral simplified wheel-rail creeping. Through the site test and the numerical calculation, the dynamic deflections and the stresses of the U-shaped girder in the Nanjing S6 Urban Rail Transit in China are obtained, and the effectiveness of the established numerical model is verified. By changing the vehicle types and speeds, the dynamic amplification coefficients (DAFs) of the vertical deflections and the biaxial stresses at the girder bottom including the key points at the plate and section intersections are calculated. The research shows that the distribution of the lateral stresses is more complex than that of the deflection and the longitudinal stresses. Based on the calculation results considering various vehicle types, it is suggested that the DAFs of the vertical deflections and the longitudinal stresses are taken as 1.30, and the DAF of the lateral stresses remains at 1.40 as stipulated by the code. The research of this paper is to provide a reference for the structural design and size optimization of the U-shaped girders for urban rail transit.

1. Introduction

As an open thin-walled structure, a U-shaped girder comprises a bottom plate carrying the track slab, two webs on both sides, and two flange plates above the webs, and all of these structural components form a "U-shape" from the cross-sectional view [1]. The structure has the advantages of low building height, good noise-reduction effect, high utilization of sectional space, fine driving safety, and beautiful appearance. As a novel type of bridge structure suitable for urban rail transit, U-shaped girder has been increasing widely used in recent years.

In the past decades, many scholars carried out research works on the static and dynamic performance of U-shaped girders. Xu et al. [2] studied the behaviour of the U-shaped thin-walled girders under the combined actions of bending, shear, and torsion and developed a method to predict the failure modes and the ultimate loads. Li et al. [3] compared the vibration and noise characteristics of the concrete

bridges with different sections by using a 3D vibroacoustic finite element method and found that the U-shaped girder generally leads to slightly lower total noise levels than the box girders. Zhang et al. [4] carried out a full-scale test to examine the ultimate bearing capacity of the U-shaped girder and developed a refined numerical model to simulate the damage evolution and the failure process. Their study shows a flexural failure occurs on the structure under the vertical loads. Xu et al. [5] observed the temperature stress of a U-shaped girder for a 48-hour period during the winter, and the research found the web, and bottom plates have significant longitudinal tensile stresses which should be considered in the design.

To design a bridge structure including the U-shaped girder, it is necessary to determine the dynamic effect of the moving vehicles on the structure [6]. In the design codes [7–9], this dynamic effect is always considered by multiplying the static live load by the dynamic amplification factor $(1 + \mu)$, in which μ is termed as the dynamic coefficient.

Generally, the DAF $(1 + \mu)$ is represented by using the ratio of dynamic response to static response. To meet the requirements of structural stiffness and cracking resistance, both the deformation and stress characteristics of the bridge structure should be considered. Ma et al. [10] investigated the DAFs of the continuous bridges by selecting 15 continuous bridges and conducting a vehicle-bridge interaction analysis, and the research indicates that the DAFs of the continuous bridges increase dramatically when resonance phenomena occur. Zhang et al. [11] analyzed the DAFs and the equivalent uniform distribution load of the bridges under the random traffic flows and adopted the Monte Carlo simulations to obtain the results of some given bridge spans. Mensinger et al. [12] studied the variations of the analytical and experimental observations on the dynamic responses of the steel railway bridge and compared the measured stresses of a locomotive passing through a historical steel railway bridge with the calculated stresses contemplating the dynamic factor proposed by EN1991-2.

The mechanical characteristics of a U-shaped girder are quite different from those of ordinary box girders. Under a vertical load, the bottom plate of a U-shaped girder not only carries the longitudinal bending moments but also has the transverse bending moments, thus producing a biaxial deflection. In 2011, Wu et al. [13, 14] carried out a field test and vehicle-bridge coupling vibration analysis to study the dynamic responses of a single-track simply supported U-shaped girder. By calculating the longitudinal and transverse stresses at the bottom plates, Wu pointed out that the differences between the DAFs of the longitudinal and transverse stresses should be considered in the design. Normally, it is convenient to use a single dynamic coefficient in structural strength and stiffness design. In China, according to the Code for Design of Urban Rail Transit Bridges (GBT51234-2017) [9], the DAF $(1 + \mu)$ is recommended to value 1.40 for the single-track U-shaped girder. However, due to the complex and different mechanical characteristics of U-shaped girder in spanning and transverse directions, using a single and conservative DAF value as done in the ordinary girder design may lead to a waste of building materials. Furthermore, the present research calculated the DAFs at only a few structural positions, and some key points at complex local positions were neglected. For the U-shaped girders, an accurate study is required considering the key points as more as possible, such as the ones at the intersection of the strengthened and unstrengthened sections in the spanning direction and at the intersections of the web and bottom plates in the transverse direction. In addition, various vehicle types with different vehicle lengths, axle weights, wheelbase, and bogie spacing are adopted on the

U-shaped girders in reality, but the existing research did not investigate the influence of vehicle types on the DAFs. Insufficient selection of the key points at complex structural local positions and overlooking the diversity of vehicle types may cause an inaccurate calculation of the DAFs. Therefore, it is necessary to conduct a thorough research on the DAFs of the U-shaped girders considering more structural positions, more vehicle types, and more study cases.

In this paper, a vehicle-bridge coupling model is established, and its effectiveness is verified through a site test. By selecting more key points at the plate and section intersections, the dynamic responses of the bridge under different vehicle types and speeds are calculated, and the DAFs of the biaxial stresses and deflections are obtained. A comprehensive analysis in this research indicates the distribution of the DAFs considering different structural positions and vehicle parameters and discusses the rationality to separate the DAF values of the deflections and the longitudinal and lateral stresses in the U-shaped girder design.

2. Vehicle-Bridge Coupling Dynamic Model

2.1. Model Description. In recent years, many research achievements have been made in the study of vehicle-bridge coupling vibration [15–17]. Based on the classical analysis methods [18], many researchers developed a series of solution methods and calculation models [19–25].

In general, a vehicle-bridge coupling model consists of the vehicle subsystem and the bridge subsystem, and they are connected by the wheel-rail interaction force. In this paper, it assumes that the wheel and rail are in a tight contact state in the vertical direction to save the calculation time. A simplified creep theory [26] is adopted to simulate the wheel-rail contact in the lateral direction, and the creep forces in the forward and swing movements of the wheel set are ignored. Only the creep force in the yaw movement of the wheel set is considered, and it equals to the product of the relative wheel-rail deformation and the creep coefficient. In this study, the creep coefficient could be obtained using the following equation:

$$c_{w-r} = -\frac{S_{22} r^{2/3}}{V} N^{2/3},\tag{1}$$

where V is the vehicle speed, N is the static axle load of the vehicle, and the parameter $S_{22} r^2/^3$ could be determined by the wheel-set radius [26].

The dynamic equation of the vehicle-bridge coupling system is

$$\begin{bmatrix} M_{vv} & 0 \\ 0 & M_{bb} \end{bmatrix} \begin{bmatrix} \ddot{X}_v \\ \ddot{X}_b \end{bmatrix} + \begin{bmatrix} C_{vv} & C_{vb} \\ C_{bv} & C_{bb} \end{bmatrix} \begin{bmatrix} \dot{X}_v \\ \dot{X}_b \end{bmatrix} + \begin{bmatrix} K_{vv} & K_{vb} \\ K_{bv} & K_{bb} \end{bmatrix} \begin{bmatrix} X_v \\ X_b \end{bmatrix} = \begin{bmatrix} F_v \\ F_b \end{bmatrix},\tag{2}$$

where the subscripts "v" and "b" represent the vehicle and the bridge.

The advantage of this method is that the motions of the vehicles and the bridge are coupled directly, and the dynamic responses of the system at each time step could be solved without any iteration to guarantee the calculation convergence.

2.1.1. Matrices of the Vehicles. There are N_v vehicles on the bridge, and their displacements could be expressed as follows:

$$X_v = \begin{bmatrix} X_{v1} & X_{v2} & \cdots & X_{vNv} \end{bmatrix}^T, \tag{3}$$

where $X_{vi} = \begin{bmatrix} X_{ci} & X_{ti1} & X_{ti2} & X_{wi11} & X_{wi12} & X_{wi21} & X_{wi22} \end{bmatrix}^T$, $(i = 1, 2, \ldots, N_v)$.

The displacements of the ith car body and its two bogies are written as follows:

$$
\begin{aligned}
X_{ci} &= \begin{bmatrix} Y_{ci} & \theta_{ci} & \psi_{ci} & Z_{ci} & \varphi_{ci} \end{bmatrix}^T, \\
X_{tij} &= \begin{bmatrix} Y_{tij} & \theta_{tij} & \psi_{tij} & Z_{tij} & \varphi_{tij} \end{bmatrix}^T, \\
X_{wijl} &= \begin{bmatrix} Y_{wijl} \end{bmatrix}^T.
\end{aligned}
\tag{4}
$$

The mass and stiffness matrices (subscript "v") of the vehicles are

$$
M_v = \begin{bmatrix}
M_{v1} & 0 & 0 & 0 \\
0 & M_{v2} & 0 & 0 \\
0 & 0 & \ddots & 0 \\
0 & 0 & 0 & M_{vNv}
\end{bmatrix},
$$

$$
K_v = \begin{bmatrix}
K_{v1} & 0 & 0 & 0 \\
0 & K_{v2} & 0 & 0 \\
0 & 0 & \ddots & 0 \\
0 & 0 & 0 & K_{vNv}
\end{bmatrix},
\tag{5}
$$

where

$$
M_{v_i} = \begin{bmatrix}
M_{c_i c_i} & 0 & 0 & 0 & 0 & 0 & 0 \\
0 & M_{t_{i1} t_{i1}} & 0 & 0 & 0 & 0 & 0 \\
0 & 0 & M_{t_{i2} t_{i2}} & 0 & 0 & 0 & 0 \\
0 & 0 & 0 & M_{w_{i11} w_{i11}} & 0 & 0 & 0 \\
0 & 0 & 0 & 0 & M_{w_{i12} w_{i12}} & 0 & 0 \\
0 & 0 & 0 & 0 & 0 & M_{w_{i21} w_{i21}} & 0 \\
0 & 0 & 0 & 0 & 0 & 0 & M_{w_{i22} w_{i22}}
\end{bmatrix}.
\tag{6}
$$

The mass matrices of the ith car body, its jth bogie, and the lth wheel set are

$$
\begin{aligned}
M_{c_i c_i} &= \begin{bmatrix} M_{c_i} & J_{c\theta_i} & M_{c\psi_i} & M_{c_i} & M_{c\varphi_i} \end{bmatrix}, \\
M_{t_{ij} t_{ij}} &= \begin{bmatrix} M_{t_{ij}} & J_{t\theta_{ij}} & M_{t\psi_{ij}} & M_{t_{ij}} & M_{t\varphi_{ij}} \end{bmatrix}, \\
M_{w_{ijl} w_{ijl}} &= \begin{bmatrix} M_{w_{ijl}} \end{bmatrix}.
\end{aligned}
\tag{7}
$$

The stiffness matrix of the ith vehicle is

$$
K_{v_i} = \begin{bmatrix}
K_{c_i c_i} & K_{c_i t_{i1}} & K_{c_i t_{i2}} & 0 & 0 & 0 & 0 \\
K_{t_{i1} c_i} & K_{t_{i1} t_{i1}} & 0 & K_{t_{i1} w_{i11}} & K_{t_{i1} w_{i12}} & 0 & 0 \\
K_{t_{i2} c_i} & 0 & K_{t_{i2} t_{i2}} & 0 & 0 & K_{t_{i2} w_{i21}} & K_{t_{i2} w_{i22}} \\
0 & K_{w_{i11} t_{i1}} & 0 & K_{w_{i11} w_{i11}} & 0 & 0 & 0 \\
0 & K_{w_{i12} t_{i1}} & 0 & 0 & K_{w_{i12} w_{i12}} & 0 & 0 \\
0 & 0 & K_{w_{i21} t_{i2}} & 0 & 0 & K_{w_{i21} w_{i21}} & 0 \\
0 & 0 & K_{w_{i22} t_{i2}} & 0 & 0 & 0 & K_{w_{i22} w_{i22}}
\end{bmatrix},
\tag{8}
$$

where

$$
K_{c_i c_i} = \begin{bmatrix}
\displaystyle\sum_{j=1}^{2} k_{2ij}^y & -\displaystyle\sum_{j=1}^{2} h_{1i} k_{2ij}^y & 0 & 0 & 0 \\[2ex]
-\displaystyle\sum_{j=1}^{2} h_{1i} k_{2ij}^y & \displaystyle\sum_{j=1}^{2}\left(h_{1i}^2 k_{2ij}^y + b_i^2 k_{2ij}^z \right) & 0 & 0 & 0 \\[2ex]
0 & 0 & \displaystyle\sum_{j=1}^{2} s_i^2 k_{2ij}^y & 0 & 0 \\[2ex]
0 & 0 & 0 & \displaystyle\sum_{j=1}^{2} k_{2ij}^z & 0 \\[2ex]
0 & 0 & 0 & 0 & \displaystyle\sum_{j=1}^{2} s_i^2 k_{2ij}^z.
\end{bmatrix},
$$

$$
K_{t_{i1} c_i} = K_{c_i t_{i1}}^T = \begin{bmatrix}
-k_{2i1}^y & -h_{1i} k_{2i1}^y & -s_i k_{2i1}^y & 0 & 0 \\
-h_{1i} k_{2i1}^y & h_{1i} h_{2i} k_{2i1}^y - b_i^2 k_{2i1}^z & -h_{2i} s_i k_{2i1}^y & 0 & 0 \\
0 & 0 & 0 & 0 & 0 \\
0 & 0 & 0 & -k_{2i1}^z & -s_i k_{2i1}^z, \\
0 & 0 & 0 & 0 & 0
\end{bmatrix},
\tag{9}
$$

$$
K_{t_{i2} c_i} = K_{c_i t_{i2}}^T = \begin{bmatrix}
-k_{2i2}^y & -h_{1i} k_{2i2}^y & s_i k_{2i2}^y & 0 & 0 \\
-h_{1i} k_{2i2}^y & h_{1i} h_{2i} k_{2i2}^y - b_i^2 k_{2i2}^z & h_{2i} s_i k_{2i2}^y & 0 & 0 \\
0 & 0 & 0 & 0 & 0 \\
0 & 0 & 0 & -k_{2i2}^z & s_i k_{2i2}^z, \\
0 & 0 & 0 & 0 & 0
\end{bmatrix},
$$

$$
K_{t_{ij} w_{ijl}} = K_{w_{ijl} t_{ij}}^T = \begin{bmatrix}
-k_{1ij}^y, \\
h_{3i} k_{1ij}^y \\
-\eta_{ijl} d_i k_{1ij}^y, \\
0 \\
0
\end{bmatrix},
$$

where k_{1ijl}^y, k_{1ijl}^z, c_{1ijl}^y, and c_{1ijl}^z are the lateral and vertical stiffness, as well as the lateral and vertical damping ratios of the primary suspension on the lth wheel set of the jth bogie of the ith vehicle. k_{2ij}^y, k_{2ij}^z, c_{2ij}^y, and c_{2ij}^z are the lateral and vertical stiffness, as well as the lateral and vertical damping ratios of the secondary suspension of the jth bogie of the ith vehicle. h_{1i}, h_{2i}, and h_{3i} are the vertical distances between the center of the car body, the axle center of the secondary suspension, and the axle center of the wheel sets of the ith car, respectively; a_i and b_i are half of the transverse distances of the primary and secondary suspension systems, and d_i and s_i are half of the longitudinal distances between the bogie centers and the bogie wheelbase of the ith car.

The damping submatrices of the vehicle could be obtained by replacing "K" with "C," and the only difference between the "K_{vi}" and "C_{vi}" is the submatrices of the wheel set:

$$
\begin{aligned}
K_{w_{ijl} w_{ijl}} &= \left[k_{1ij}^y \right], \\
C_{w_{ijl} w_{ijl}} &= \left[c_{1ij}^y + c_{w-r} \right].
\end{aligned}
\tag{10}
$$

2.1.2. Matrices of the Bridge. The number of the mode shapes considered in the calculation is N_b, and the generalized displacements can be expressed as follows:

$$
X_b = \begin{bmatrix} q_1 & q_2 & \cdots & q_{Nb} \end{bmatrix}^T.
\tag{11}
$$

The mass, stiffness, and damping submatrices of the bridge (subscript "bb") are

$$M_{bb} = \begin{bmatrix} 1+M_b^{11} & M_b^{12} & \cdots & M_b^{1N_b} \\ M_b^{21} & 1+M_b^{22} & \cdots & M_b^{2N_b} \\ \cdots & \cdots & \ddots & \cdots, \\ M_b^{N_b1} & M_b^{N_b2} & \cdots & 1+M_b^{N_bN_b} \end{bmatrix}, \quad (12)$$

where $M_b^{nm} = \sum_{i=1}^{N_v}\sum_{j=1}^{2}\sum_{l=1}^{2}[\phi_{\theta ijl}^n\phi_{\theta ijl}^m J_{ijl} + \phi_{zijl}^n\phi_{zijl}^m m_{ijl}]$

$$K_{bb} = \begin{bmatrix} \omega_1^2+K_b^{11} & K_b^{12} & \cdots & K_b^{1N_b} \\ K_b^{21} & \omega_2^2+K_b^{22} & \cdots & K_b^{2N_b} \\ \cdots & \cdots & \ddots & \cdots, \\ K_b^{N_b1} & K_b^{N_b2} & \cdots & \omega_{N_b}^2+K_b^{N_bN_b} \end{bmatrix}, \quad (13)$$

where $K_b^{nm} = \sum_{i=1}^{N_v}\sum_{j=1}^{2}\sum_{l=1}^{2}[\phi_{\theta ijl}^n\phi_{\theta ijl}^m k_{1ij}^y a_i^2 + \phi_{zijl}^n\phi_{zijl}^m k_{1ij}^z]$.

$$C_{bb} = \begin{bmatrix} 2\xi\omega_1+C_b^{11} & C_b^{12} & \cdots & C_b^{1N_b} \\ C_b^{21} & 2\xi\omega_1+C_b^{22} & \cdots & C_b^{2N_b} \\ \cdots & \cdots & \ddots & \cdots, \\ C_b^{N_b1} & C_b^{N_b2} & \cdots & 2\xi\omega_{N_b}+C_b^{N_bN_b} \end{bmatrix},$$
$$(14)$$

where $C_b^{nm} = \sum_{i=1}^{N_v}\sum_{j=1}^{2}\sum_{l=1}^{2}[(\phi_{yijl}^n + h_{4i}\phi_{\theta ijl}^n)(\phi_{yijl}^m + h_{4i}\phi_{\theta ijl}^m) c_{w-r} + \phi_{\theta ijl}^n\phi_{\theta ijl}^m c_{1ij}^y a_i^2 + \phi_{zijl}^n\phi_{zijl}^m c_{1ij}^z]$.

2.1.3. Matrices of Vehicle-Bridge Interaction.
The stiffness matrices coupling the vehicles and the bridge (subscripts "vb" and "bv") could be expressed as follows:

$$K_{vb} = K_{bv}^T = \begin{bmatrix} K_{v_1b} \\ K_{v_2b} \\ \cdots, \\ K_{v_{Nv}b} \end{bmatrix},$$

$$K_{v_ib} = \begin{bmatrix} 0 & 0 & \cdots & 0 \\ K_{t_{i1}q_1} & K_{t_{i1}q_2} & \cdots & K_{t_{i1}q_{Nb}} \\ K_{t_{i2}q_1} & K_{t_{i2}q_2} & \cdots & K_{t_{i2}q_{Nb}} \\ K_{w_{i11}q_1} & K_{w_{i11}q_2} & \cdots & K_{w_{i11}q_{Nb}} \\ K_{w_{i12}q_1} & K_{w_{i12}q_2} & \cdots & K_{w_{i12}q_{Nb}} \\ K_{w_{i21}q_1} & K_{w_{i21}q_2} & \cdots & K_{w_{i21}q_{Nb}} \\ K_{w_{i22}q_1} & K_{w_{i22}q_2} & \cdots & K_{w_{i22}q_{Nb}} \end{bmatrix}, \quad (15)$$

where the submatrices coupling the jth bogie of the ith vehicle and the generalized displacement of the nth mode of the bridge are

$$K_{t_{ij}q_n} = K_{t_{ij}q_n}^T = -\sum_{l=1}^{2} \begin{bmatrix} 0 \\ \phi_{\theta ijl}^{nm}a_i^2 k_{1ij}^y \\ 0 \\ (\phi_{zijl}^{nm} + e\phi_{\theta ijl}^{nm})k_{1ij}^z. \\ \eta_{ijl}d_i\phi_{zijl}^{nm}k_{1ij}^z \end{bmatrix}. \quad (16)$$

Similarly, the damping submatrix of the vehicle could also be obtained from equations (19)–(22) by replacing the "K" with "C."

$$\begin{aligned} K_{w_{ijl}q_n} &= K_{q_nw_{ijl}} = [0], \\ C_{w_{ijl}q_n} &= C_{q_nw_{ijl}} = -[(\phi_{zijl}^{nm} + h_{4i}\phi_{\theta ijl}^{nm})c_{1ij}^y], \end{aligned} \quad (17)$$

where $i = 1, 2, \ldots, N_v$; $n = 1,2, \ldots, N_b$; $j = 1,2$.

2.1.4. Forces on the Vehicle-Bridge System
(1) Forces on the vehicles

$$F_v = \begin{bmatrix} F_{v_1} & F_{v_2} & \cdots & F_{v_{Nv}} \end{bmatrix}^T, \quad (18)$$

where

$$F_{v_i} = \begin{bmatrix} 0 & F_{t_{i1}} & F_{t_{i2}} & F_{w_{i11}} & F_{w_{i12}} & F_{w_{i21}} & F_{w_{i22}} \end{bmatrix}^T,$$

$$F_{t_{ij}} = \sum_{l=1}^{2} \begin{bmatrix} 0 \\ a_i^2[k_{1ij}^y\theta_s(x_{ijl}) + c_{1ij}^y\dot\theta_s(x_{ijl})], \\ 0 \\ k_{1ij}^z Z_s(x_{ijl}) + c_{1ij}^z\dot Z_s(x_{ijl}), \\ \eta_{ijl}d_i[k_{1ij}^z Z_s(x_{ijl}) + c_{1ij}^z\dot Z_s(x_{ijl})]. \end{bmatrix},$$

$$F_{w_{ijl}} = [c_{w-r}\dot Y_s(x_{ijl})]. \quad (19)$$

(2) Forces on the bridge

$$F_b = \begin{bmatrix} F_{q_1} & F_{q_2} & \cdots & F_{q_{Nb}} \end{bmatrix}^T, \quad (20)$$

where

$$\begin{aligned} F_{q_n} = \sum_{i=1}^{N_v}\sum_{j=1}^{2}\sum_{l=1}^{2}\Big\{&-[\phi_{\theta ijl}^n a_i^2 k_{1ij}^z\theta_S(x_{ijl}) + (\phi_{zijl}^n + e\phi_{\theta ijl}^n)k_{1ij}^z Z_S(x_{ijl})], \\ &-[\phi_{\theta ijl}^n a_i^2 c_{1ij}^z\dot\theta_S(x_{ijl}) + (\phi_{zijl}^n + e\phi_{\theta ijl}^n)c_{1ij}^z\dot Z_S(x_{ijl})], \\ &-[(\phi_{yijl}^n + h_{4i}\phi_{\theta ijl}^n)c_{w-r}\dot Y_S(x_{ijl})] + \phi_{zijl}^n\big(0.25M_{c_i} + 0.5M_{t_{ij}} + M_{w_{ijl}}\big)\Big\}. \end{aligned} \quad (21)$$

In the previous equation, the values of $\phi_{yijl}^n(x_{ijl})$, $\phi_{\theta ijl}^n(x_{ijl})$, and $\phi_{zijl}^n(x_{ijl})$ represent, in the nth mode shape, the lateral, torsional, and vertical modal displacements at the location x_{ijl}, where the lth wheel set of the jth bogie of the ith vehicle arrives. $\theta_s(x_{ijl})$ and $Z_s(x_{ijl})$ are the rotational and vertical track irregularities at the wheel-set location x_{ijl}. $\dot{Y}_S(x_{ijl})$, $\dot{\theta}_S(x_{ijl})$, and $\dot{Z}_S(x_{ijl})$ are the velocities of the lateral, rotational, and vertical irregularities at x_{ijl}, and they are equal to the slopes of the relative irregularities divided by the vehicle speed. These modal displacements and irregularities change when the vehicle moves on the bridge, so that the dynamic equation of the vehicle-bridge system becomes linear differential equations with time-varying coefficients. In this study, the equations are solved by using the Newmark-β method.

2.2. Model Verification

2.2.1. Project Introduction.
Taking the 30 m prestressed concrete (PC) simply supported U-shaped girder in Nanjing S6 Urban Rail Transit as a study case, a series of site tests and numerical simulations was carried out. The height of the girder is 1.80 m, and the bottom width is 3.91 m. The thicknesses of the bottom plates at the midspan and the girder end are 260 mm and 400 mm, respectively. The key cross sections of the girder are shown in Figure 1.

To consider the stress diffusion on the track slab as well as the spatial mechanical characteristics of the U-shaped girder, a 3D finite element model of the U-shaped girder including the track slab is established using the ANSYS software, as shown in Figure 2.

By the eigenvalue calculation, the frequencies and the mode shapes of the 1st~5th modes are obtained and shown in Table 1.

The train formation is "motor + trailer + trailer + motor," and the running speed during the test is 110 km/h. Due to the data lack of the track irregularities, the US six-level spectrum is used to generate the irregularities in lateral (alignment), rotational (cross level), and vertical (longitudinal level) directions, as shown in Figure 3.

The key cross sections at the 1/4, 1/2, and 3/4 spans of the girder where the maximum responses may usually appear are considered in the calculation. Moreover, the responses of the cross sections near the movable and fixed ends should also be checked. To take a more accurate analysis than the previous work, hundreds of key points are selected along the girder. A local rectangular coordinate system is created, by which all of the key points could be expressed more clearly, as shown in Figure 4(a). In the transverse direction, there are 13 sets of lateral coordinates (y_1~y_{13}) including the intersections of the web and bottom plates, as shown in Figure 4(b). In the spanning direction, there are 17 sets of longitudinal

coordinates (x_1~x_{17}) including the intersections of the strengthened sections near midspan and unstrengthened sections near girder end, as shown in Figure 4(c).

2.2.2. Results Comparison.
To verify the established vehicle-bridge analysis model, a site test was carried out on a U-shaped girder in Nanjing S6 Urban Rail Transit. Due to the limitation on the number of measuring points in the test, only a few of the key points with the x-coordinate of x_1, x_7, x_9, x_{11}, x_{17} and with the y-coordinate of y_1, y_4, y_7, y_{10}, y_{13} in Figure 4 are selected as the measuring points. In the site test, the vehicles are type-B metro trains with empty loaded, and the weights of the empty motor and trailer cars are 9.0t and 8.25t, respectively. To record the dynamic vertical deflections of the girder, the multipoint video detection system of HPQN-X was adopted in the test site, as shown in Figure 5(a).

At the same time, using the INV3062V high-precision acquisition instrument shown in Figure 5(b) as the dynamic strain collecting tool, combined with the INV2312N wireless static strain measuring instrument shown in Figure 5(c) to eliminate the additional static strains such as the thermal strain, the vehicle-induced strains at the girder bottom were obtained.

(1) Vertical Deflection. The time histories of the vertical deflections d_z at the transverse centers of the bottom plate as well as the intersections of the web and the bottom plates at the 1/4, 1/2, and 3/4 spans are calculated and compared with the test data, as shown in Figure 6.

By comparing the previous figures, it can be observed that the vertical deflections at the midspan are the largest, and those at the 1/4 span are the smallest. On the same cross section, the deflections at the intersections on both sides are almost equivalent to those at the transverse center. The comparison demonstrates that the calculated and measured time histories are in good agreement.

(2) Strain at Girder Bottom. On the cross sections at the 1/4, 1/2, and 3/4 spans and near the girder ends, the longitudinal strains ε_X and the lateral strains ε_Y at the measuring points are plotted with the test values, as shown in Figure 7.

From the calculation results, it is clear that the stresses at the transverse centers of the bottom plate gradually increase from the girder ends to the midspan, and the increasing trend slows near the midspan. In most cases, the longitudinal stresses are greater than the lateral ones.

By comparing the test and calculation results, it can be found that they are close, which proves that the vehicle-bridge coupling dynamic model established in this paper could be used to predict the structural deflections and stresses under different vehicle speeds. The stress distribution on the U-shaped girder is very complex, and a detailed analysis of the DAF is always required.
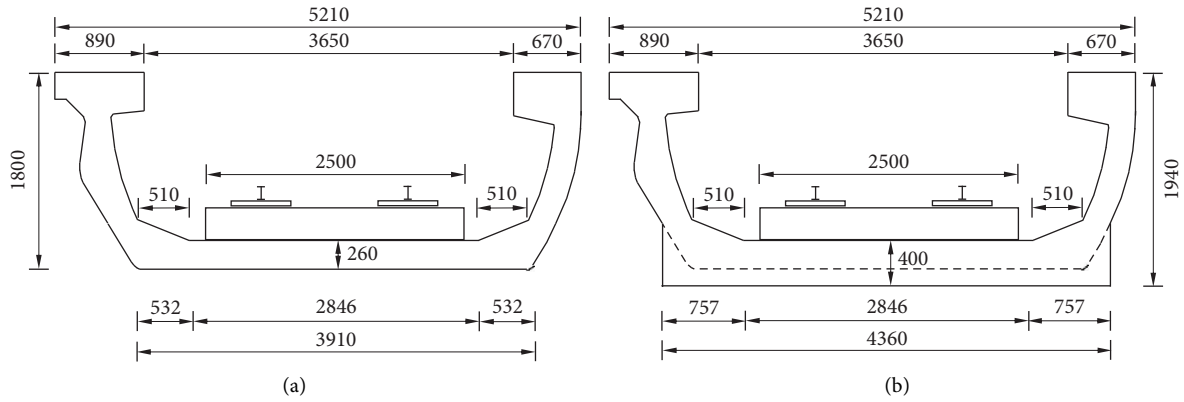
Figure 1: Cross sections of the 30 m U-shaped girder (unit: mm): (a) midspan and (b) girder end.

Figure 2: Finite element model of the U-shaped girder.

Table 1: Dynamic characteristics of the U-shaped girder.

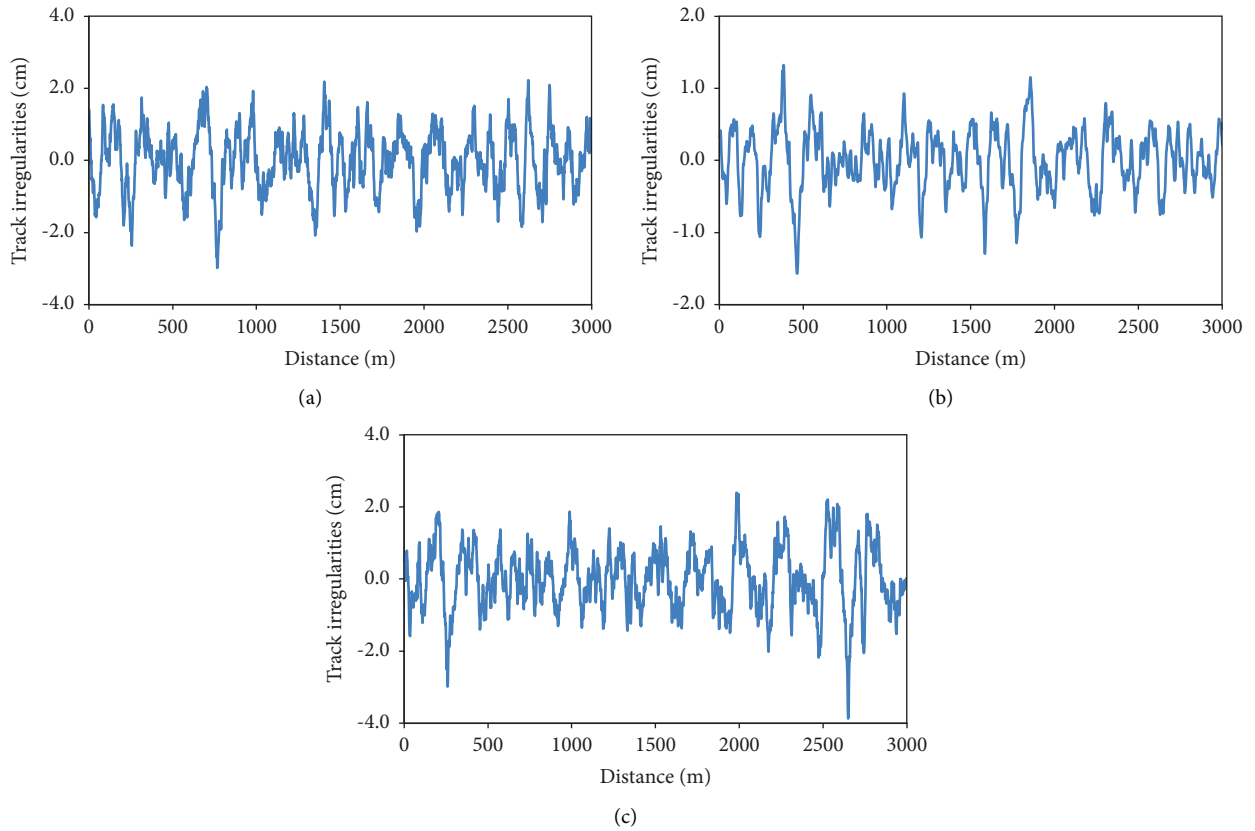| No.	Frequencies (Hz)	Mode shapes	Descriptions
1	3.971		The 1st vertical bending
2	6.680		The 1st lateral bending
3	12.670		The 2nd vertical bending
4	12.797		The 1st rotation
5	17.006		The 2nd lateral bending

(a)

(b)

(c)

FIGURE 3: Track irregularities: (a) alignment, (b) cross level, and (c) longitudinal level.

(a)

(b)

(c)
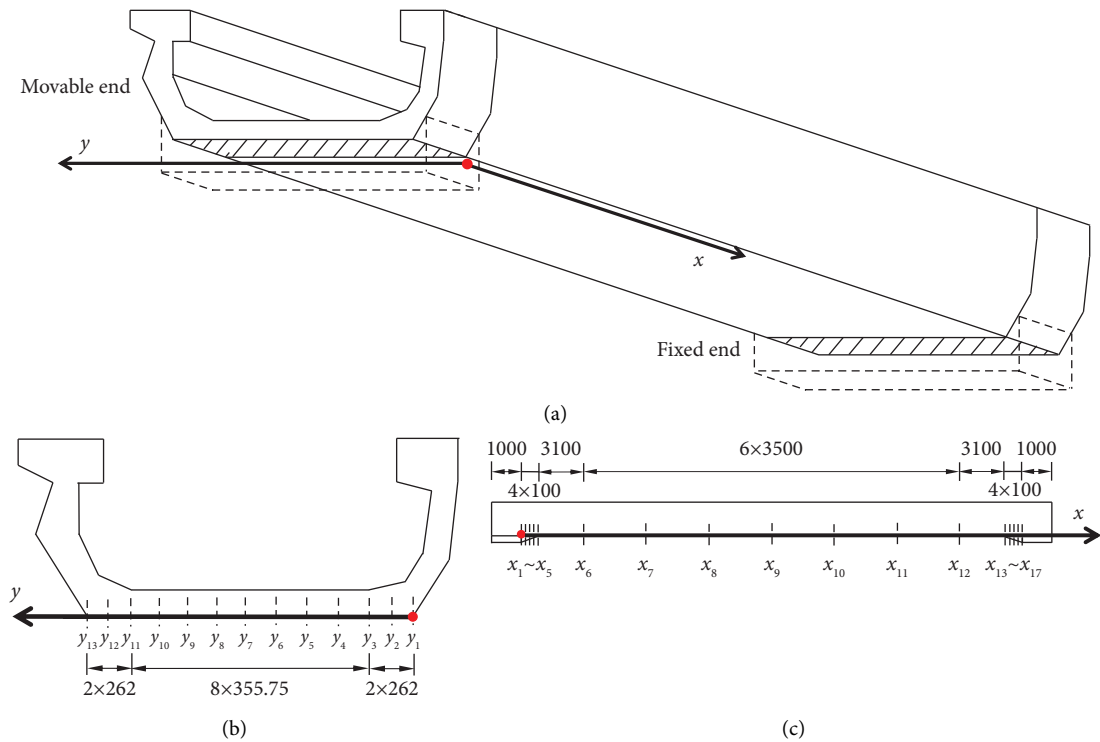
FIGURE 4: Key-point locations along the U-shaped girder: (a) the local rectangular coordinate system defined in the study, (b) transverse direction, and (c) spanning direction.

(a)

(b)

(c)
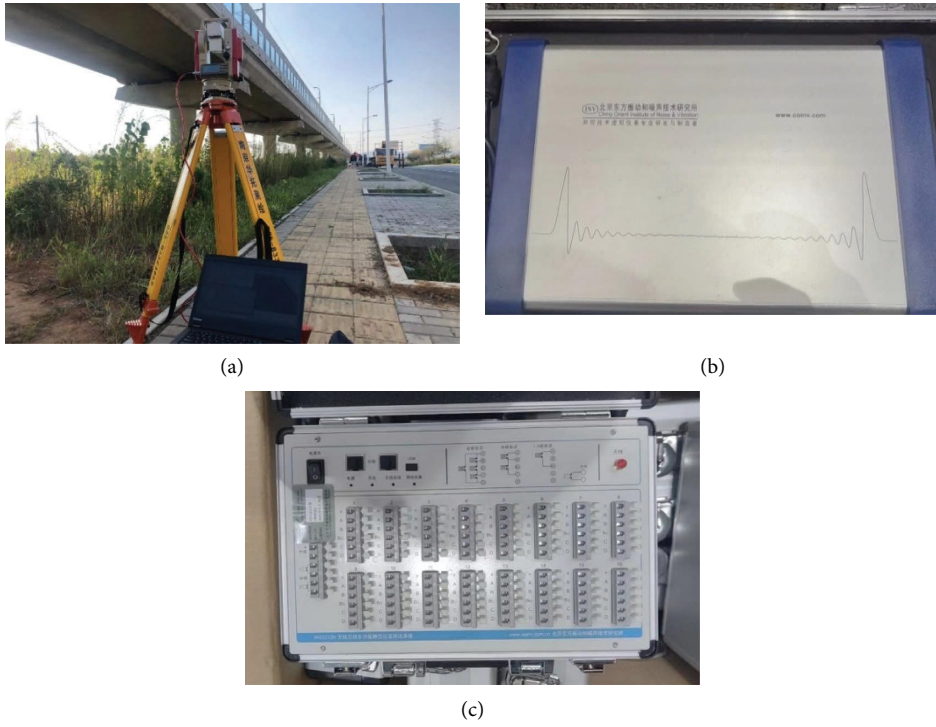
FIGURE 5: Measuring instruments used in the site test: (a) displacement detection system of HPQN-X, (b) acquisition instrument of INV3062V, and (c) strain measuring instrument of INV2312N.
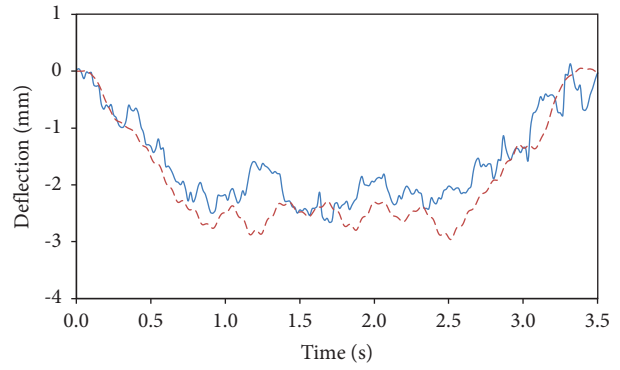

(a)

(b)

(c)
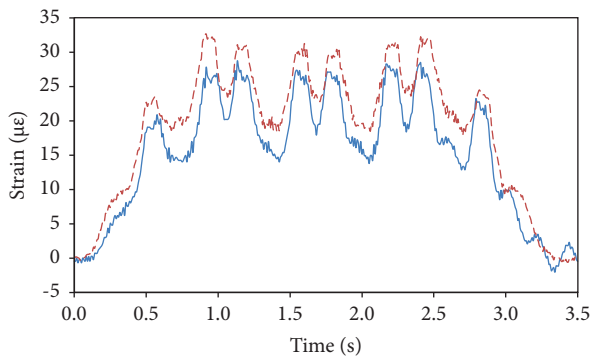
(d)
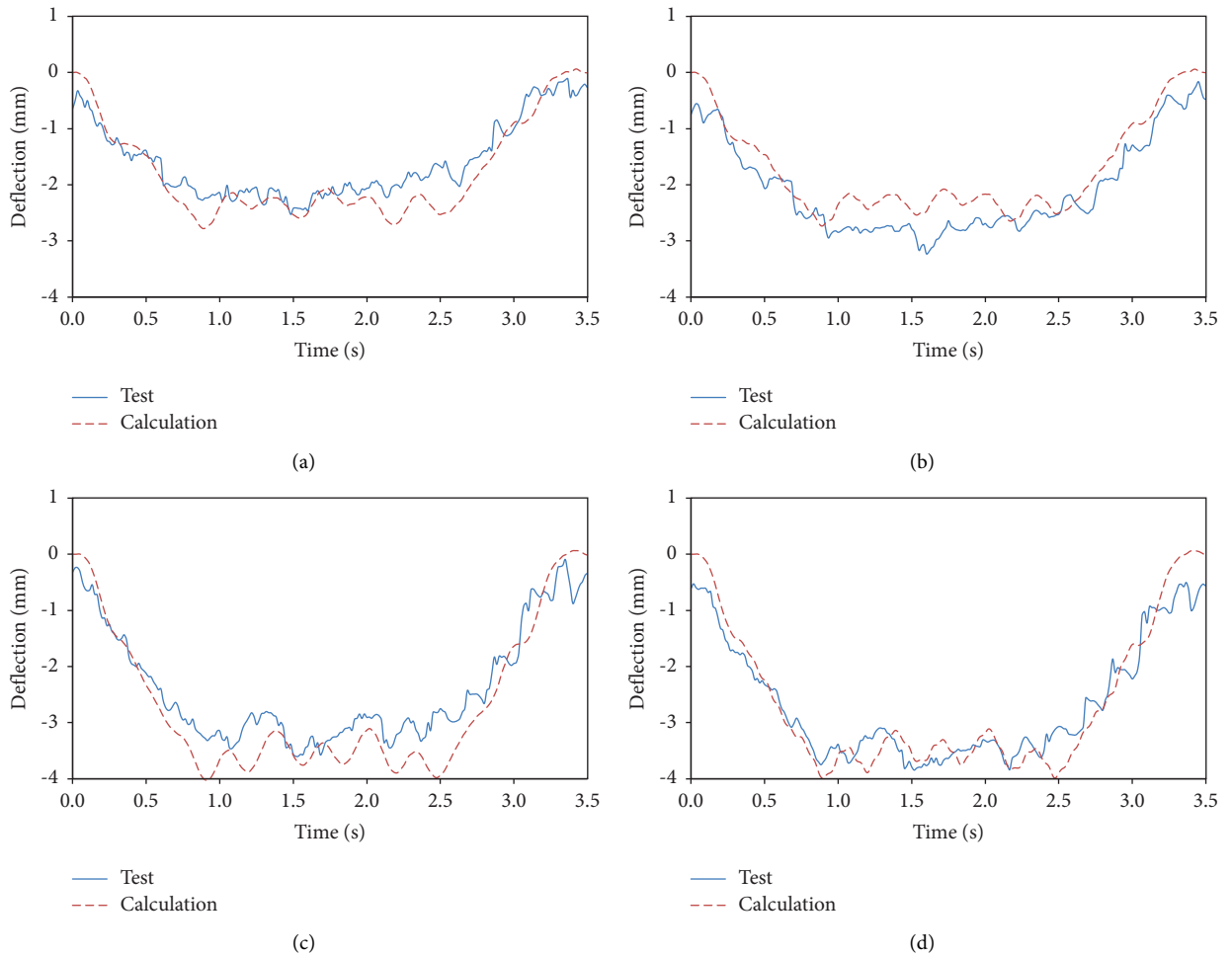
FIGURE 6: Continued.
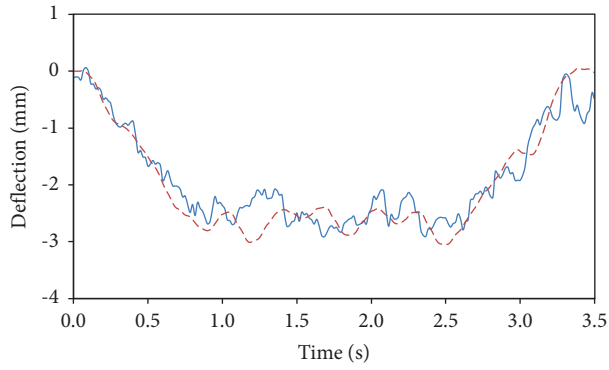
(e)

(f)

FIGURE 6: Time histories of the measured and calculated deflections: (a) d_Z at the location of (x_7, y_7), (b) d_Z at the location of (x_7, y_{13}), (c) d_Z at the location of (x_9, y_7), (d) d_Z at the location of (x_9, y_1), (e) d_Z at the location of (x_{11}, y_7), and (f) d_Z at the location of (x_{11}, y_{13}).
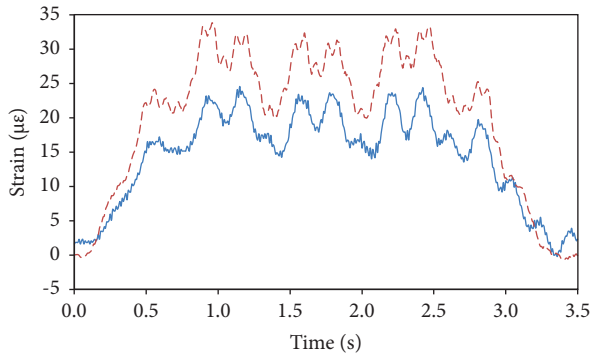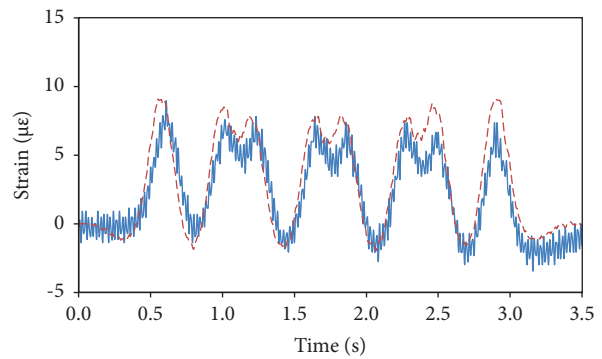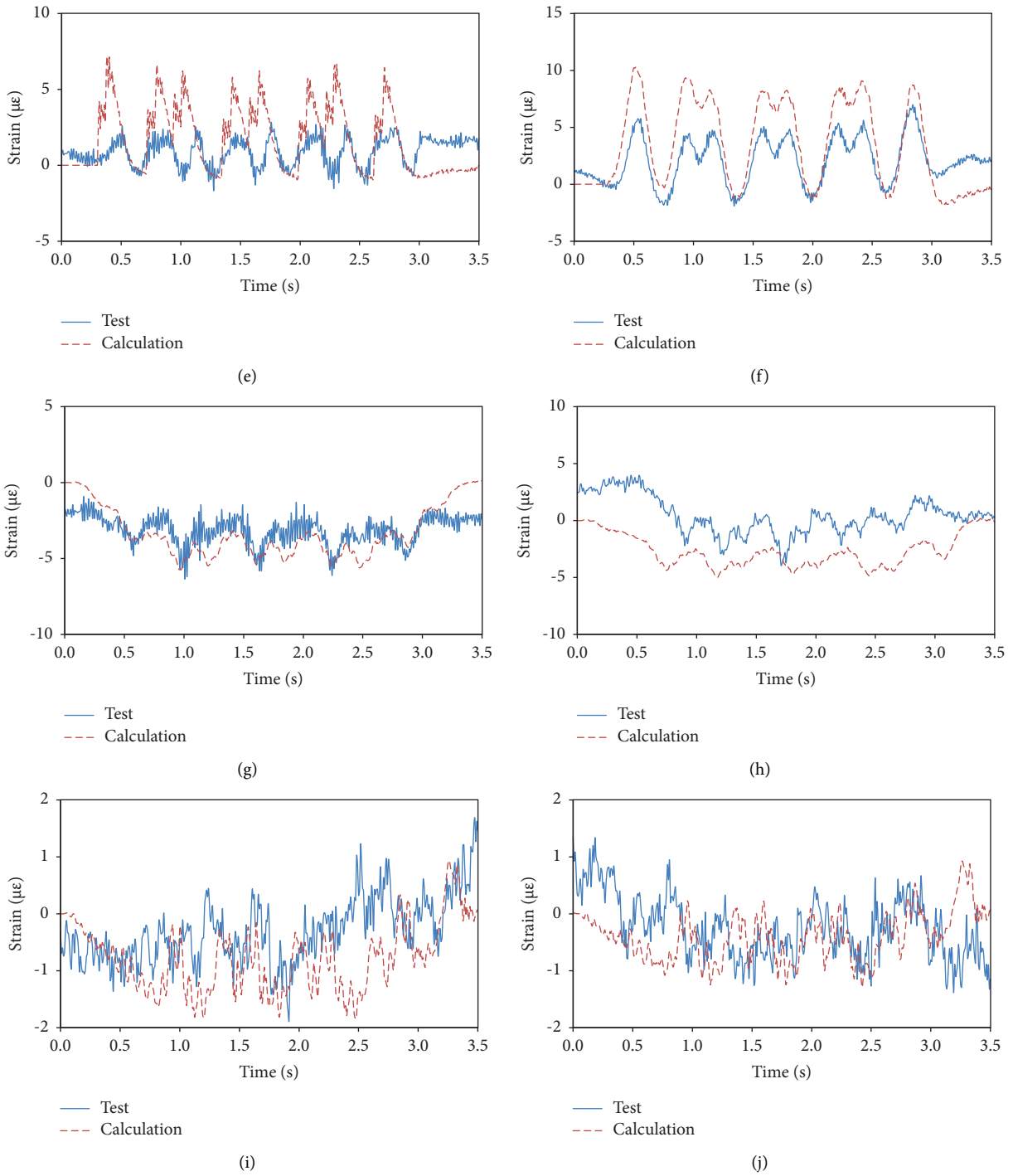

(a)
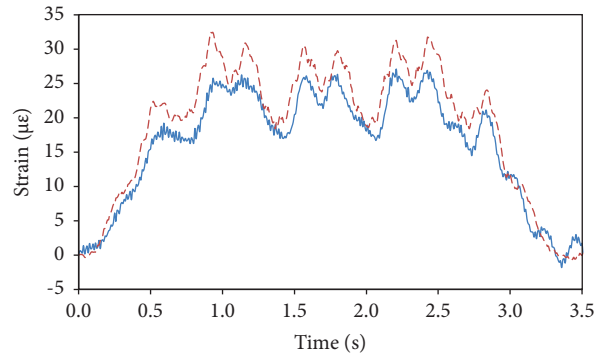
(b)

(c)

(d)

FIGURE 7: Continued.

(e)

(f)

(g)

(h)

(i)

(j)

FIGURE 7: Time histories of the measured and calculated strains: (a) ε_X at the location of (x_9, y_{13}), (b) ε_X at the location of (x_9, y_1), (c) ε_X at the location of (x_9, y_7), (d) ε_Y at the location of (x_9, y_7), (e) ε_Y at the location of (x_1, y_7), (f) ε_Y at the location of (x_7, y_7), (g) ε_Y at the location of (x_9, y_1), (h) ε_Y at the location of (x_{11}, y_{13}), (i) ε_Y at the location of (x_{17}, y_{13}), and (j) ε_Y at the location of (x_{17}, y_1).

3. Case Study

3.1. Dynamic Responses

(1) Vertical Deflection. For railway and metro bridges, an excessive structural deformation will cause severe vibration or even vehicle derailment on the bridge, and the structural deformation caused by the live load should be limited. The time histories of the vertical deflections at the key points are calculated, and the results when the type-B vehicle runs at the operation speed of 120 km/h are listed in Figure 8.

By comparing the time histories in Figure 8, it is clear that the closer the midspan, the greater the deflection. At the midspan, the deflections exceed 6.0 mm. For the deflections on the same cross sections, their difference is not obvious.

(2) Longitudinal Stress. For most girder structures, the longitudinal stresses at the girder bottom are normally greater than the lateral ones, and it is generally necessary to consider the longitudinal stresses when determining the DAF. The time histories of the longitudinal stresses σ_X when the type-B vehicle runs at 120 km/h are listed in Figure 9.

From the time histories in Figure 9, it can be found that the bottom of the girder carries longitudinal tensile stresses at the 1/4, 1/2, and 3/4 spans during the vehicle passing through. The maximum tensile stress is close to 2.0 MPa, appearing at the midspan. The girder bottom is mainly in compression near the girder ends, and the maximum stress near the fixed end is greater than that near the movable end.

(3) Lateral Stress. The lateral stresses are mainly caused by the transverse bending of the girder, and the analysis of these stresses is essential to determine the DAF of the U-shaped girder. When the speed of the type-B vehicle is 120 km/h, the time histories of the lateral stresses σ_Y are listed in Figure 10.

Comparing Figure 10 with Figure 9, it can be observed that the distribution of the lateral stresses is more complicated than that of the longitudinal stresses, although the amplitudes of the lateral stresses are lower than the longitudinal ones in most cases. In most cases, the girder experiences both tensile and compressive stresses. At the 1/4, 1/2, and 3/4 spans, the key points with y_3, y_4, y_{10}, and y_{11} coordinates have the greatest lateral tensile stress, meaning that the most unfavourable positions are near the transverse midspan of the bottom plate. Near the girder ends, the key points with y_1~y_4 and y_{10}~y_{13} coordinates near the intersection areas are in compression, and the ones near the transverse center of the bottom plate are mainly in tension.

3.2. The DAFs.
In this study, the DAF is defined as follows:

$$\text{DAF} = 1 + \mu = \frac{D_{\text{dy}}}{D_{\text{st}}}, \tag{22}$$

where D_{dy} is the structural dynamic response caused by the moving vehicle and D_{st} is the structural static response caused by the design live load of the vehicle.

The quasistatic loading is taken by moving the vehicle at a low speed of 1.0 km/h, and the corresponding responses are set to be D_{st}. By using the vehicle-bridge coupling model introduced in Section 2, the calculated dynamic responses D_{dy} could be obtained. To conduct a thorough study of the DAFs, the vehicles including the type-A, type-B, and type-D subway trains are considered, and all of them are widely used in China [9]. Due to the difference between the lengths, the wheelbases, the bogie spacings, and the axle weights of the vehicles, the structural dimensions of the girders for various vehicle types are different. The information on the vehicles and girders is shown in Table 2.

Where, the intervals of y3~y11 are 8×368.25 mm and 8×393.25 mm, for the girders designed for the type-A and type-D trains, respectively.

Through a series of calculations, the DAFs of the U-shaped girder under different cases can be obtained. Table 3 shows the distribution of the DAFs of the girder designed for the type-A vehicle at speeds of 80 km/h, 100 km/h, 120 km/h, 140 km/h, and 160 km/h.

From Table 3, it is clear that the DAFs of the deflections are all lower than 1.10 in all listed cases. Similarly, most of the DAFs of the longitudinal stresses do not exceed 1.10, except for those at the strengthened section close to the fixed end. For the DAFs of the lateral stresses, the values are greater than 1.10 at many key points along the girder, and the maximum DAF of 1.320 appears at the left plate intersection of the 1/4 span when $V = 120$ km/h.

Table 4 shows the distribution of the DAFs of the girder designed for the type-B vehicle at the speeds of 80 km/h, 100 km/h, 120 km/h, 140 km/h, and 160 km/h.

By observing Table 4, it is found that the DAFs of the deflections and the longitudinal stresses are around 1.20 when the vehicle speed $V > 120$ km/h. From the distribution trend in the figures, the average DAFs of the lateral stresses increase with the vehicle speed, and the values at some positions exceed 1.20 when $V \geq 120$ km/h. At the left plate intersection of the 1/4 span, the maximum DAF reaches 1.385.

Table 5 shows the distribution of the DAFs of the girder designed for the type-D vehicle at the speeds of 120 km/h, 140 km/h, 160 km/h, 180 km/h, and 200 km/h.

It is clearly seen from Table 5 that the DAFs of the deflections and the longitudinal stresses are greater than the cases of type-A and type-B because of the higher speed range for the type-D train. At the listed speeds, the DAFs greater than 1.20 are mainly at the strengthened section close to the fixed end. Although the operation speed of the type-D train is clearly higher than others, the DAFs of the lateral stresses are still less than the stipulated value of 1.40 in the code.
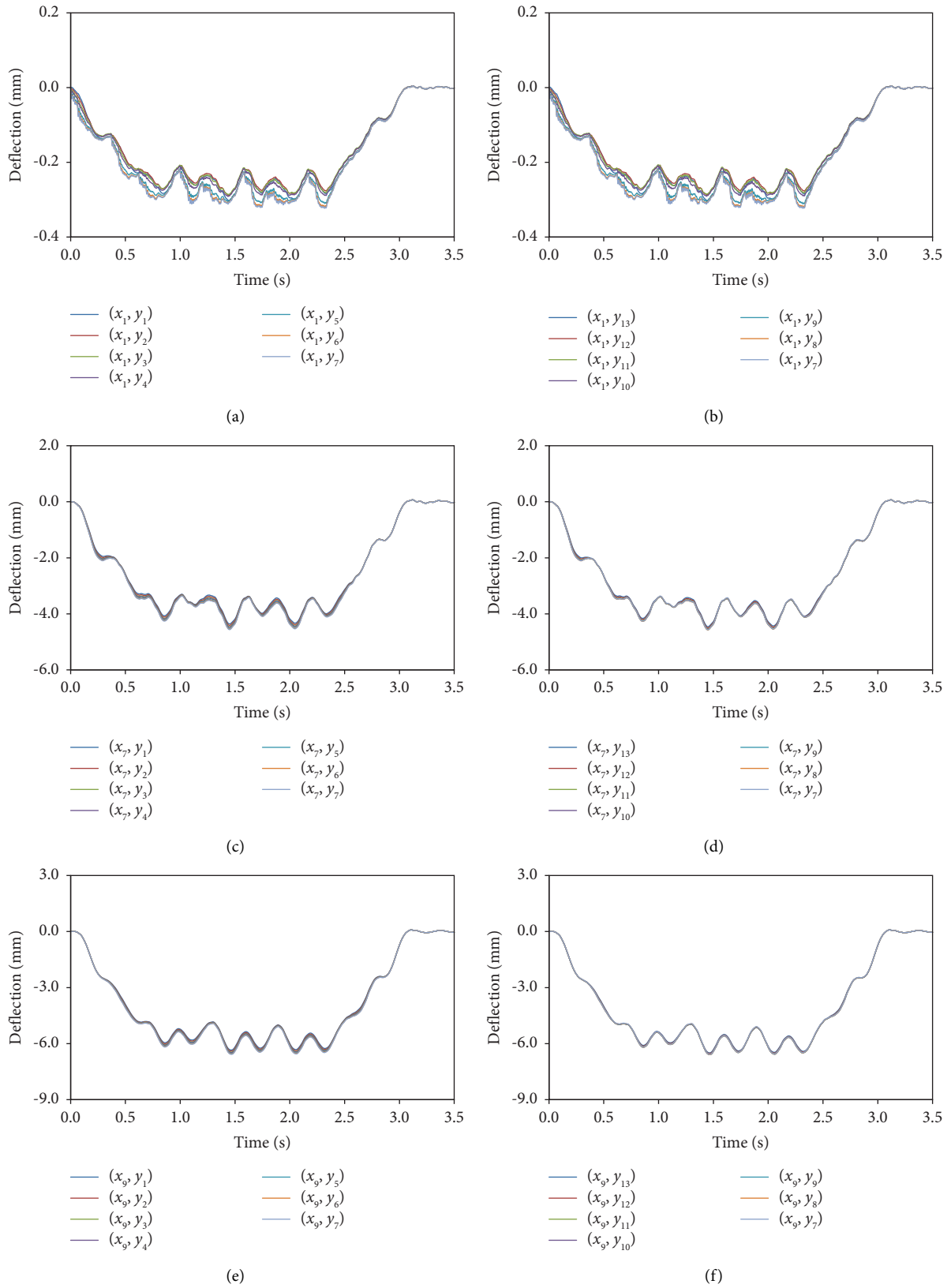
(a)

(b)

(c)

(d)

(e)

(f)

Figure 8: Continued.
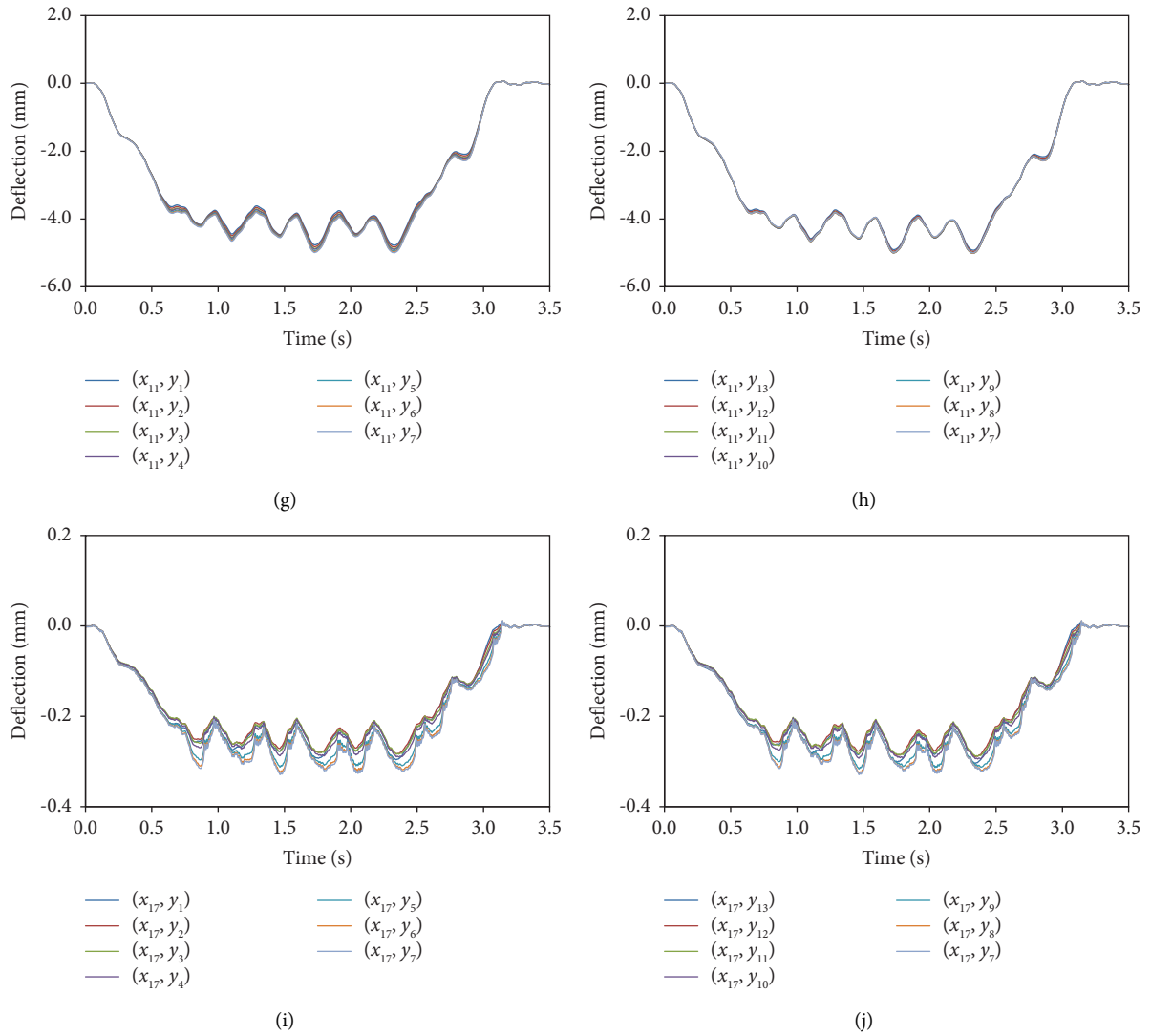
(g)

(h)

(i)

(j)

Figure 8: Time histories of the vertical deflections at the bottom plate ($V = 120$ km/h): (a) d_Z at the locations of $(x_1, y_1 \sim y_7)$, (b) d_Z at the locations of $(x_1, y_7 \sim y_{13})$, (c) d_Z at the locations of $(x_7, y_1 \sim 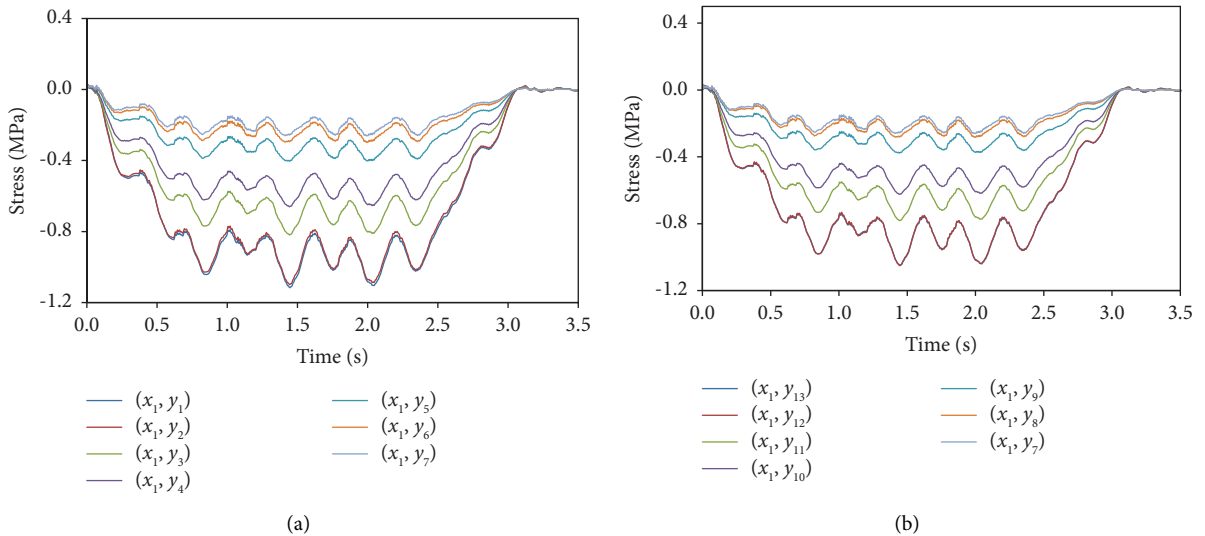y_7)$ (d) d_Z at the locations of $(x_7, y_7 \sim y_{13})$, (e) d_Z at the locations of $(x_9, y_1 \sim y_7)$, (f) d_Z at the locations of $(x_9, y_7 \sim y_{13})$, (g) d_Z at the locations of $(x_{11}, y_1 \sim y_7)$, (h) d_Z at the locations of $(x_{11}, y_7 \sim y_{13})$, (i) d_Z at the locations of $(x_{17}, y_1 \sim y_7)$, and (j) d_Z at the locations of $(x_{17}, y_7 \sim y_{13})$.
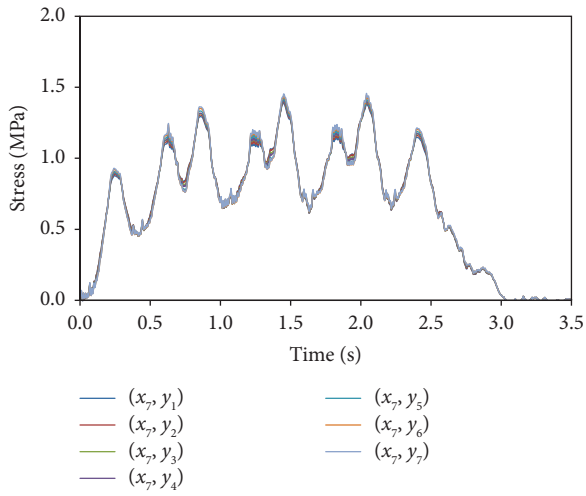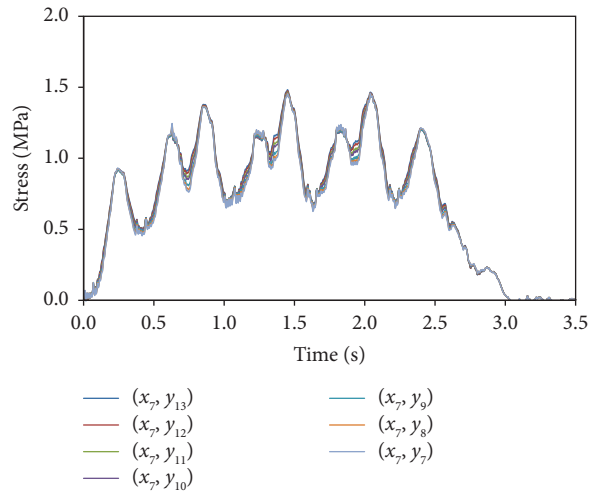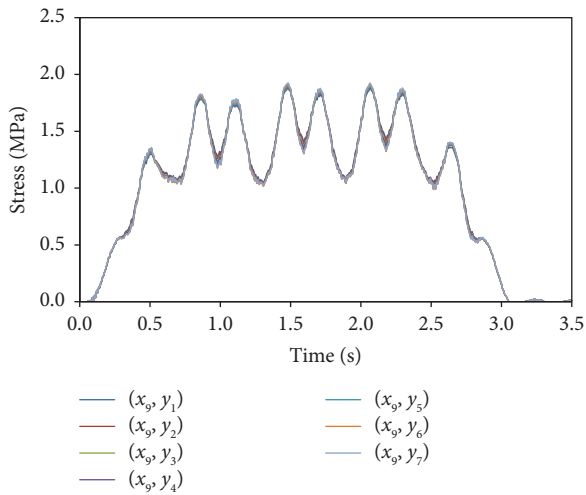

(a)

(b)

Figure 9: Continued.
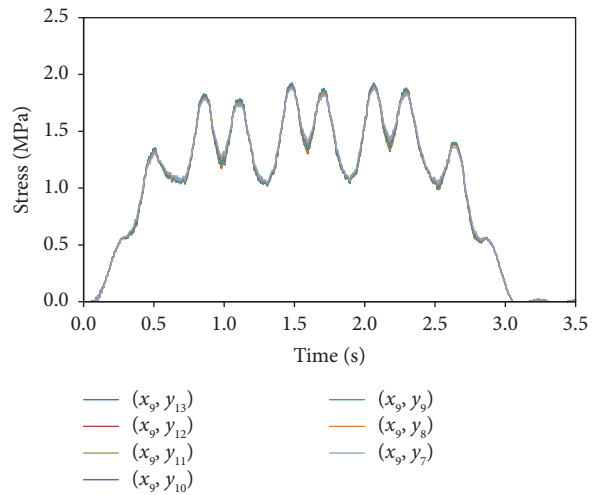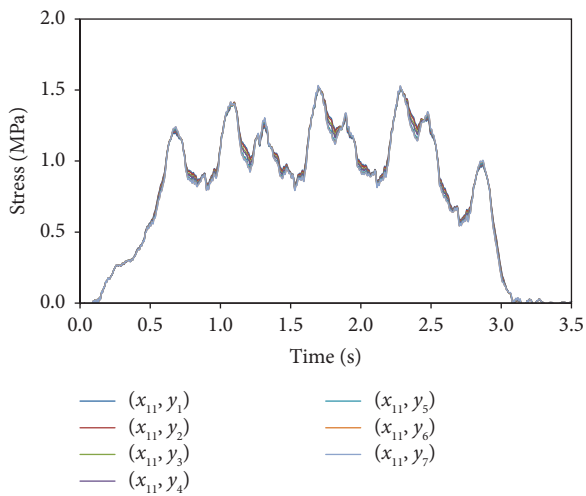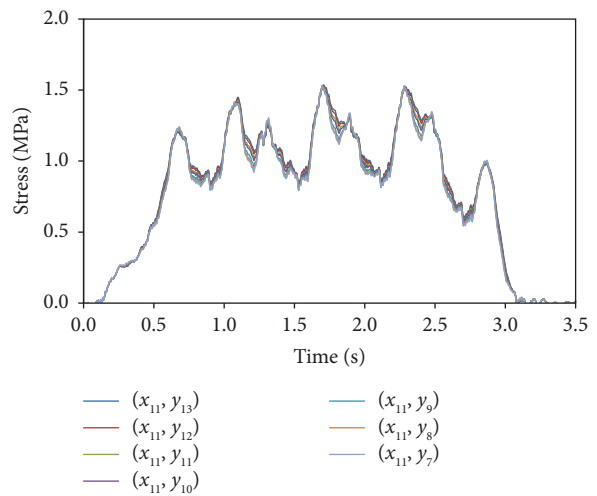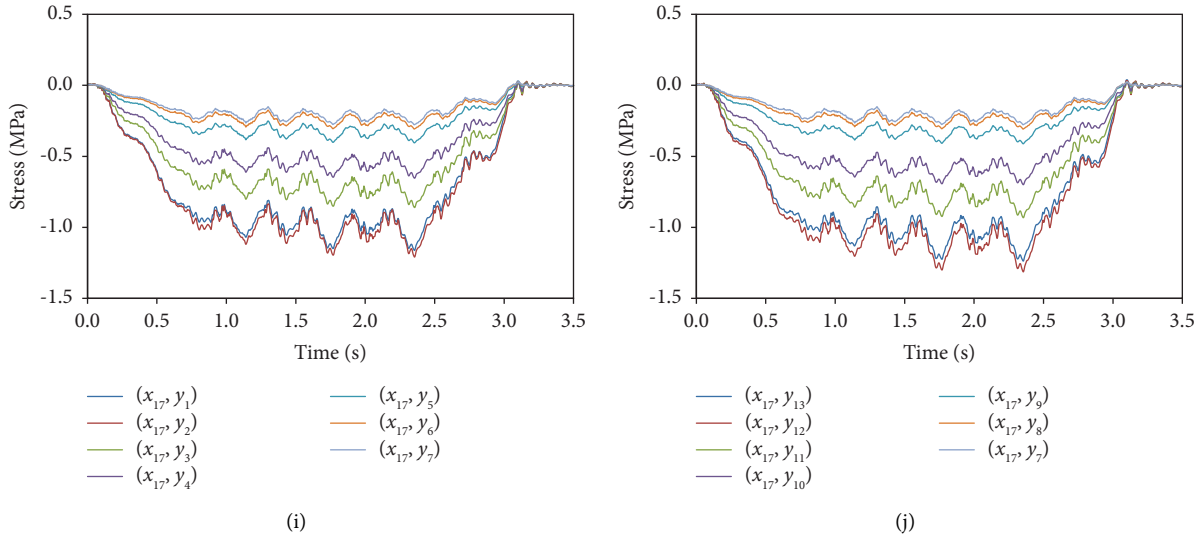
(c)

(d)

(e)

(f)

(g)

(h)

Figure 9: Continued.

(i)

(j)

Figure 9: Time histories of the longitudinal stresses at the bottom plate ($V = 120$ km/h): (a) σ_X at the locations of ($x_1, y_1 \sim y_7$), (b) σ_X at the locations of ($x_1, y_7 \sim y_{13}$), (c) σ_X at the locations of ($x_7, y_1 \sim y_7$), (d) σ_X at the locations of ($x_7, y_7 \sim y_{13}$), (e) σ_X at the locations of ($x_9, y_1 \sim y_7$), (f) σ_X at the locations of ($x_9, y_7 \sim y_{13}$), (g) σ_X at the locations of ($x_{11}, y_1 \sim y_7$), (h) σ_X at the locations of ($x_{11}, y_7 \sim y_{13}$), (i) σ_X at the locations of ($x_{17}, y_1 \sim y_7$), and (j) σ_X at the locations of ($x_{17}, y_7 \sim y_{13}$).
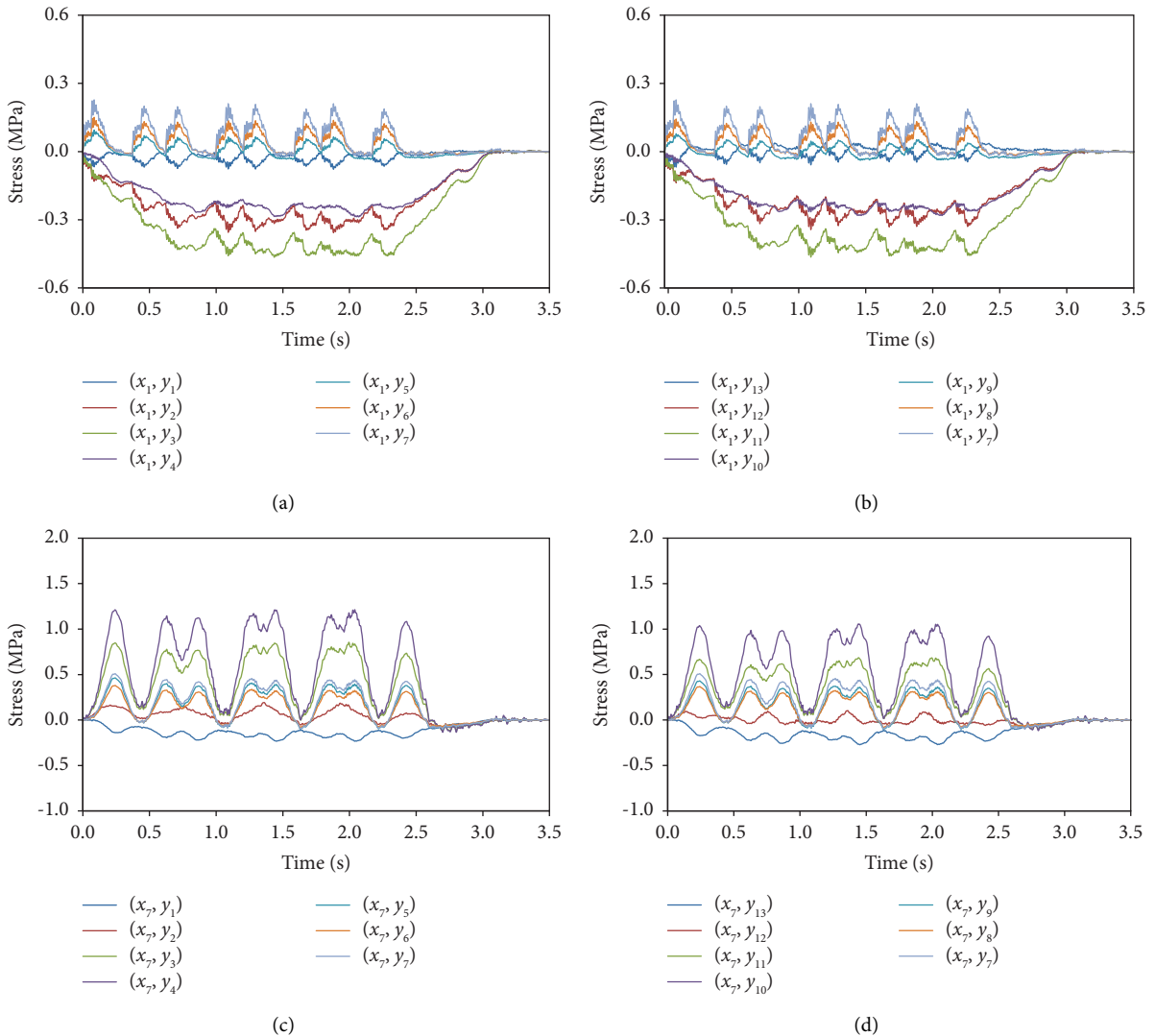

(a)
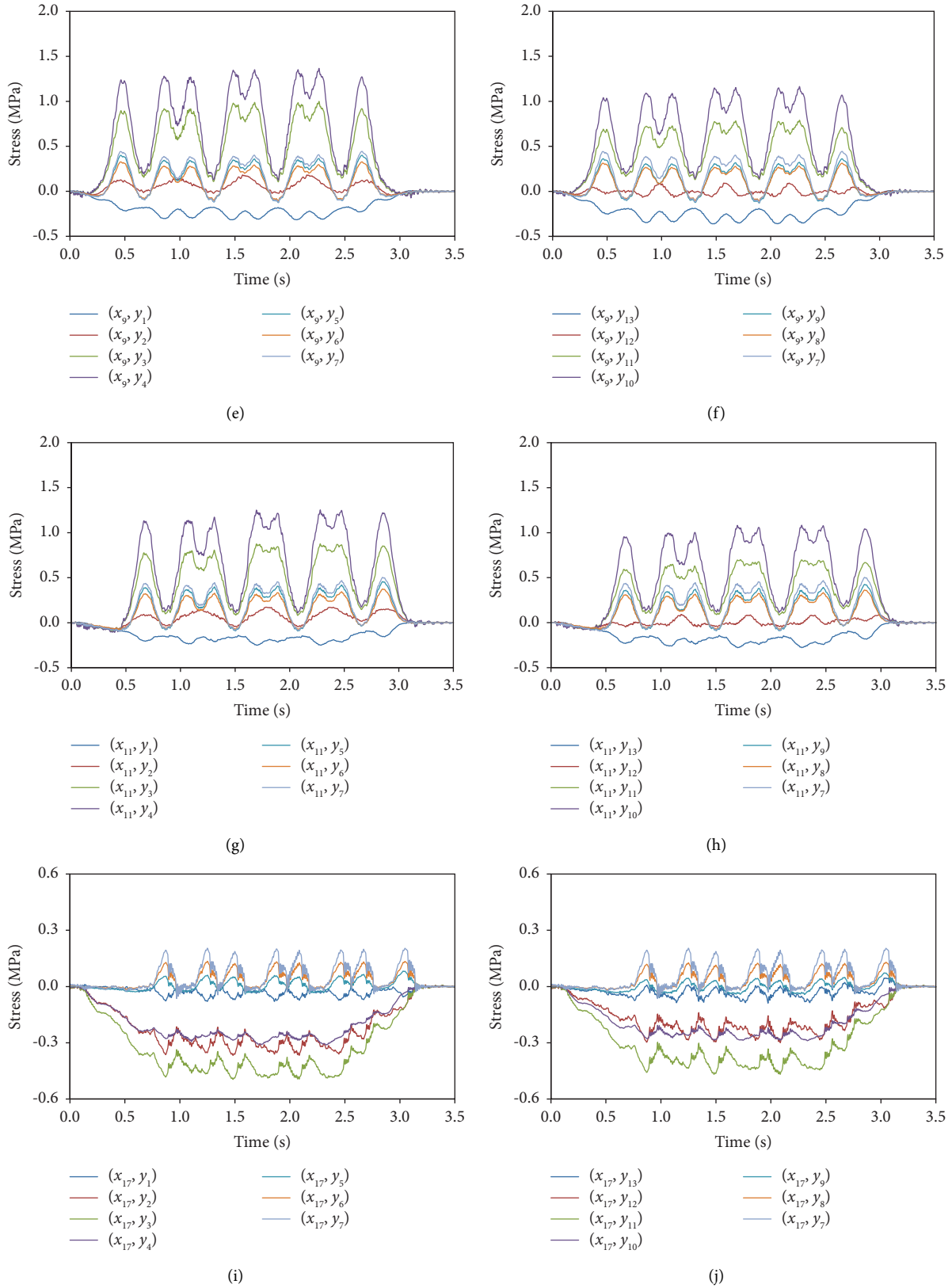
(b)

(c)

(d)

Figure 10: Continued.

FIGURE 10: Time histories of the lateral stresses at the bottom plate ($V = 120$ km/h): (a) σ_Y at the locations of (x_1, $y_1 \sim y_7$), (b) σ_Y at the locations of (x_1, $y_7 \sim y_{13}$), (c) σ_Y at the locations of (x_7, $y_1 \sim y_7$), (d) σ_Y at the locations of (x_7, $y_7 \sim y_{13}$), (e) σ_Y at the locations of (x_9, $y_1 \sim y_7$), (f) σ_Y at the locations of (x_9, $y_7 \sim y_{13}$), (g) σ_Y at the locations of (x_{11}, $y_1 \sim y_7$), (h) σ_Y at the locations of (x_{11}, $y_7 \sim y_{13}$), (i) σ_Y at the locations of (x_{17}, $y_1 \sim y_7$), and (j) σ_Y at the locations of (x_{17}, $y_7 \sim y_{13}$).

TABLE 2: Dimensions of the vehicles and the corresponding girders.

Train types	Vehicle dimensions (unit: m)	Structural dimensions (unit: mm)
A	(a) Motor car (axle weight: 16.00t) (b) Trailer car (axle weight: 15.40t)	(a) Midspan (b) Girder end
B	(a) Motor car (axle weight: 14.00t) (b) Trailer car (axle weight: 13.83t)	(a) Midspan (b) Girder end

TABLE 2: Continued.

Train types	Vehicle dimensions (unit: m)	Structural dimensions (unit: mm)

(a) Motor car (axle weight: 17.00*t*)

(a) Midspan

D

(b) Trailer car (axle weight: 16.25*t*)

(b) Girder end

To follow the conservative principles in structural design, the maximum calculated speeds of the vehicles in this study are set to be 40 km/h higher than the operation speeds. In the calculation, the vehicle speed is increased gradually from half of the operation speed to the maximum calculated speed (with an increment of 10 km/h). Tables 6–8 list the maximum DAFs of all study cases.

From the summarized results in Tables 6–8, it can be concluded that the maximum DAFs of different responses occur at the girder designed for different vehicle types; thus, the vehicle types should not be neglected in the DAF calculation. For the maximum calculated speeds in this study, the maximum DAFs of the vertical deflections and the longitudinal stresses are 1.251 and 1.262, appearing in the study cases of the type-D train. The maximum DAF of the lateral stresses is 1.385, and it occurs in the study case of the type-A train. For the operation speeds, the related maximum DAFs of these three responses are 1.127, 1.164, and 1.302, respectively. As it is known, a lower DAF means a smaller live load applied on the girder, thus may lead to a reduction of the girder dimensions, especially a reduction in the thickness of the bottom plate. Considering the redundancy in vehicle speed and structural design, the DAFs of the vertical deflections and longitudinal stresses representing the longitudinal mechanical characteristics are suggested as 1.30, and the DAF of the lateral stresses is still taken as 1.40. As suggested, a separate definition of the DAFs in longitudinal and lateral directions may cause a lower live load when checking the longitudinal stresses, and it will be beneficial in reasonable dimension optimization and effective material saving.

Table 3: Distribution of the DAFs of the U-shaped girder designed for the type-A vehicle.

V	Vertical deflection	Longitudinal stress	Lateral stress
80			
100			
120			
140			
160			

(■ 1.0~1.1; ■ 1.1~1.2; ■ 1.2~1.3; ■ 1.3~1.4).
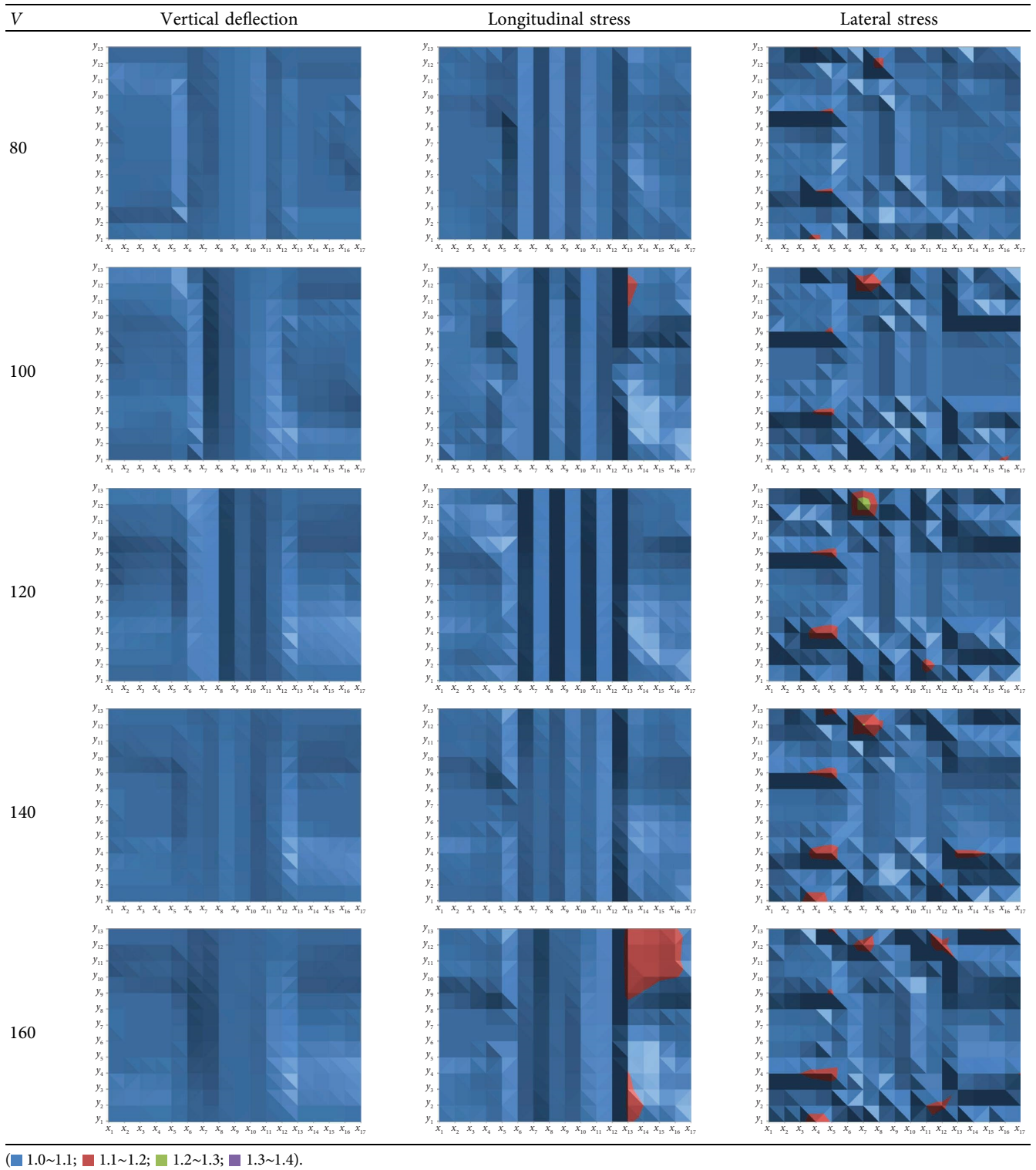
TABLE 4: Distribution of the DAFs of the U-shaped girder designed for the type-B vehicle.

■ 1.0~1.1; ■ 1.1~1.2; ■ 1.2~1.3; ■ 1.3~1.4.
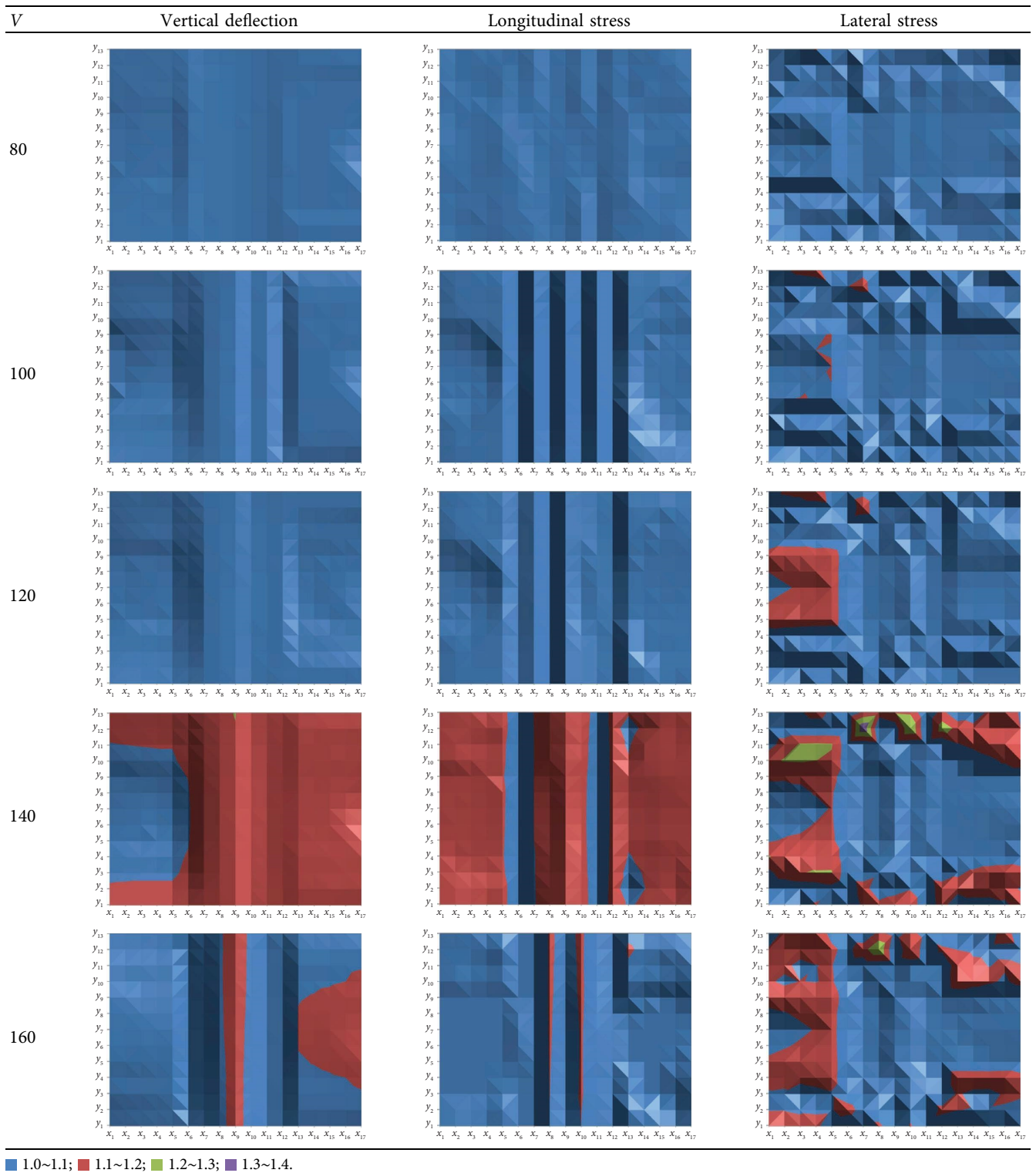
TABLE 5: Distribution of the DAFs of the U-shaped girder designed for the type-D vehicle.

■ 1.0~1.1; ■ 1.1~1.2; ■ 1.2~1.3; ■ 1.3~1.4.

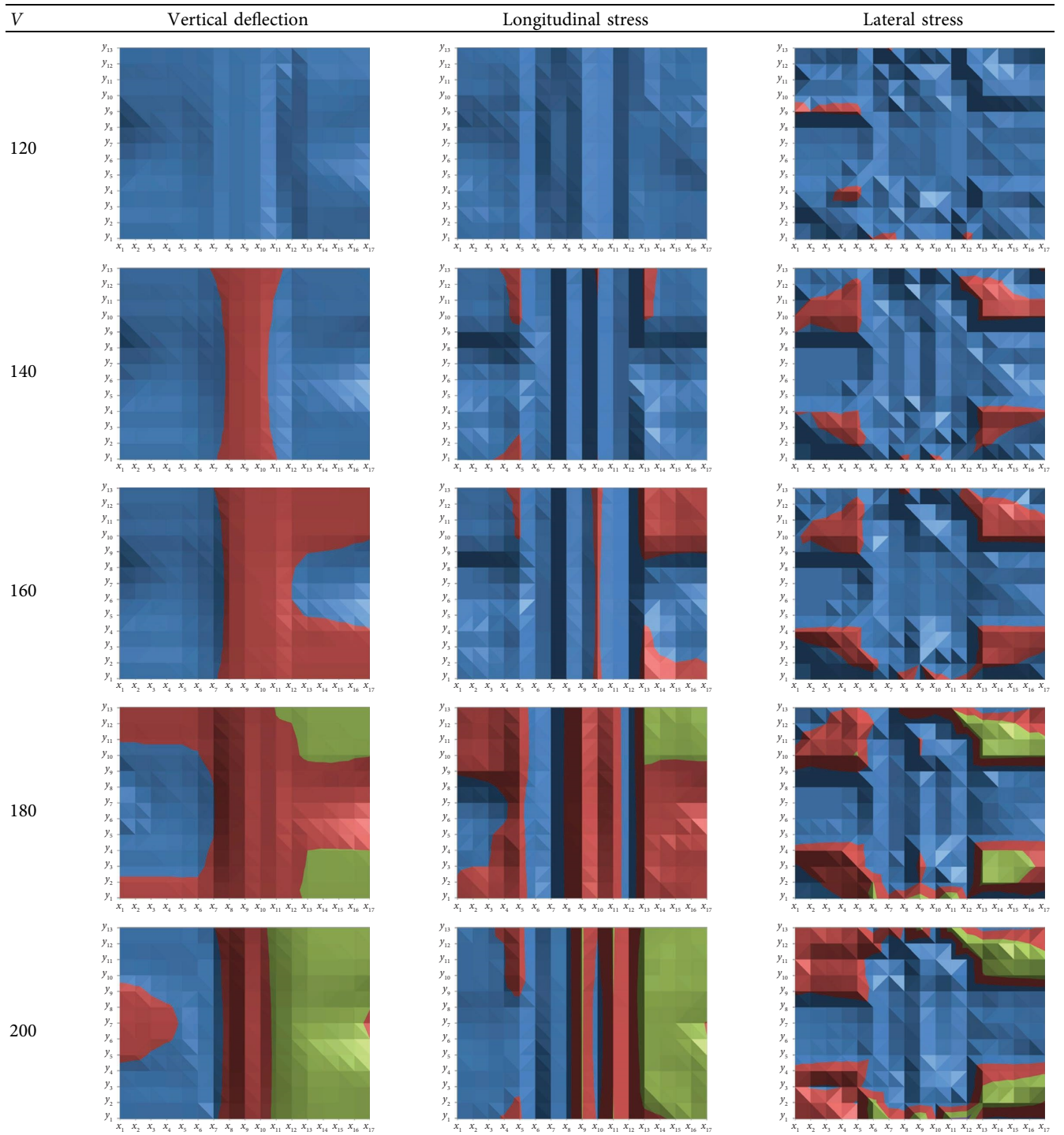TABLE 6: The DAFs of the vertical deflections.

	Train speed (km/h)										
Type-A	60	70	80	90	100	110	120	130	140	150	160
	1.013	1.012	1.033	1.044	1.069	1.096	1.078	1.060	1.050	1.045	1.077
Type-B	60	70	80	90	100	110	120	130	140	150	160
	1.009	1.015	1.023	1.051	1.084	1.062	1.069	1.125	1.201	1.182	1.119
Type-D	100	110	120	130	140	150	160	170	180	190	200
	1.027	1.042	1.080	1.106	1.113	1.113	1.127	1.163	1.206	1.234	1.251
Max	1.251 (at the left plate intersection near the fixed end of the girder designed for type-D with $V = 200$ km/h)										

TABLE 7: The DAFs of the longitudinal stresses.

	Train speed (km/h)										
Type-A	60	70	80	90	100	110	120	130	140	150	160
	1.028	1.022	1.040	1.060	1.105	1.118	1.092	1.065	1.067	1.085	1.123
Type-B	60	70	80	90	100	110	120	130	140	150	160
	1.028	1.030	1.034	1.054	1.089	1.071	1.092	1.129	1.197	1.175	1.112
Type-D	100	110	120	130	140	150	160	170	180	190	200
	1.038	1.045	1.087	1.108	1.114	1.146	1.164	1.191	1.215	1.222	1.263
Max	1.263 (at the transverse center near the fixed end of the girder designed for type-D with $V = 200$ km/h)										

TABLE 8: The DAFs of the lateral stresses.

	Train speed (km/h)										
Type-A	60	70	80	90	100	110	120	130	140	150	160
	1.092	1.085	1.139	1.122	1.185	1.175	1.302	1.253	1.211	1.228	1.156
Type-B	60	70	80	90	100	110	120	130	140	150	160
	1.094	1.104	1.106	1.098	1.142	1.160	1.208	1.225	1.385	1.347	1.292
Type-D	100	110	120	130	140	150	160	170	180	190	200
	1.104	1.128	1.140	1.136	1.162	1.170	1.160	1.214	1.304	1.305	1.328
Max	1.385 (at the left plate intersection of the 1/4 span of the girder designed for type-B with $V = 140$ km/h)										

4. Conclusions

Based on the vehicle-bridge coupling dynamics theory, the DAFs of the deflections and stresses of the U-shaped girder are analyzed by the field test and numerical calculation. Through a comprehensive study considering the local positions at the web and plate intersections and the diversity of the vehicle types, the distribution of the DAFs is studied. The results show the followings:

(1) The girder bottom is in longitudinal tensile at the 1/4, 1/2, and 3/4 spans, and it is in longitudinal compression near the girder ends. For the key points along the transverse direction of the same cross sections, the difference between the vertical deflections or the longitudinal stresses is small. Although the amplitudes of the lateral stresses are lower than the longitudinal ones, the stress distribution is more complex, and there are both lateral tensile and compressive stresses at the girder bottom.

(2) The maximum DAFs considering the type-A, type-B, and type-D vehicles are different, and the influence of the vehicle types could not be neglected in the DAF calculation. After incorporating the results of various vehicle types, the maximum DAFs of the vertical deflections and the longitudinal stresses appear at the left plate intersection near the fixed end, and the maximum one of the lateral stresses is at the left plate intersection of the 1/4 span. As a key position with the clear significant DAF values, the intersection of the web and bottom plates should be concerned carefully when checking cracking resistance.

(3) For the operation vehicle speeds, the maximum DAFs of the vertical deflections, the longitudinal stresses, and lateral stresses are 1.127, 1.164, and 1.302. For the maximum calculated speeds 40 km/h higher than the operation ones, the maximum DAFs of the related responses are 1.251, 1.262, and 1.385, respectively. Considering the redundancy principle in structural design, it is suggested that the DAFs of the vertical deflections and the longitudinal stresses are taken as 1.30, and the DAF of the lateral stresses remains 1.40 as stipulated by the code.

Data Availability

The data used to support the findings of this study are included within the article.

Conflicts of Interest

The authors declare that there are no conflicts of interest.

Acknowledgments

References

[1] A. R. Cusens and J. L. Rounds, "Tests of a U-beam bridge deck," *Structure Engineering*, vol. 51, pp. 377–382, 1973.

[2] J. C. Xu, B. Diao, Q. Q. Guo, Y. H. Ye, Y. L. Mo, and H. B. Chen, "Interaction of bending, shear and torsion in U-shaped thin-walled RC girders," *Engineering Structures*, vol. 179, pp. 655–669, 2019.

[3] Q. Li, B. R. Dai, Z. H. Zhu, and D. J. Thompson, "Comparison of vibration and noise characteristics of urban rail transit bridges with box-girder and U-shaped sections," *Applied Acoustics*, vol. 186, 2022.

[4] J. F. Zhang, Y. Jing, P. D. Li, W. S. Han, N. Zhang, and Y. L. Zhou, "Experimental and numerical investigation on the ultimate vertical bearing capacity of U-shaped girder with damaged web," *Sensors*, vol. 19, no. 17, p. 3735, 2019.

[5] D. Xu, G. F. Sun, and G. N. Xu, "Study on the influence of negative temperature gradient of U-shaped girder of rail transit in winter," *Journal of Physics: Conference Series*, vol. 1549, no. 4, 2017.

[6] P. Paultre, O. Chaallal, and J. Proulx, "Bridge dynamics and dynamic amplification factors a review of analytical and experimental findings," *Canadian Journal of Civil Engineering*, vol. 19, no. 2, pp. 260–278, 1992.

[7] Aashto, *The American Association of State Highway and Transportation Officials*, Washington, D. C, 2020.

[8] *Code for Design on Railway Bridge and Culvert (TB 10002 2017)*, China railway publishing house, Beijing, China, 2017.

[9] *Code for Design of Urban Rail Transit Bridge (GBT51234 2017)*, China Architecture & Building Press, Beijing, China, 2017.

[10] L. Ma, W. Zhang, W. S. Han, and J. X. Liu, "Determining the dynamic amplification factor of multi-span continuous box girder bridges in highways using vehicle-bridge interaction analyses," *Engineering Structures*, vol. 181, no. 15, pp. 47–59, 2019.

[11] Q. L. Zhang, A. Vrouwenvelder, and J. Wardenier, "Dynamic amplification factors and EUDL of bridges under random traffic flows," *Engineering Structures*, vol. 23, no. 6, pp. 663–672, 2001.

[12] M. Mensinger, R. R. Fard, A. Hacker, and A. Näßl, "Validation of the dynamic amplification factor in case of historic railway steel bridges with short and medium spans," *Procedia Engineering*, vol. 156, pp. 233–240, 2016.

[13] L. Q. Wu, D. J. Wu, and Q. Li, "Vehicle-bridge dynamic response analysis of U-girder for urban rail transit," *Journal of Railway Science and Engineering*, vol. 7, no. 6, pp. 6–11, 2010.

[14] L. Q. Wu, D. J. Wu, and Q. Li, "Experimental study on vehicle-bridge dynamic characteristics of thin-walled trough girder bridge for urban rail transit," *China Railway Science*, vol. 32, no. 4, pp. 31–37, 2011.

[15] Y. B. Yang, J. D. Yau, and Y. S. Wu, *Vehicle-bridge Interaction Dynamics with Application to High-Speed Railways*, World Scientific Publisher, Singapore, 2004.

[16] W. M. Zhai and H. Xia, *Train-Track-Bridge Dynamic Interaction: Theory and Engineering Application*, Science Press, Beijing, 2011.

[17] H. Xia, N. Zhang, and W. W. Guo, *Dynamic Interaction of Train-Bridge Systems in High-Speed Railways: Theory and Application*, Springer Nature, London, 2018.

[18] W. M. Zhai, Z. L. Han, Z. W. Chen, L. Ling, and S. Y. Zhu, "Train–track–bridge dynamic interaction: a state-of-the-art review," *Vehicle System Dynamics*, vol. 57, no. 7, pp. 984–1027, 2019.

[19] N. Zhang and H. Xia, "Dynamic analysis of coupled vehicle-bridge system based on inter-system iteration method," *Computers & Structures*, vol. 114-115, pp. 26–34, 2013.

[20] P. Xiang, Z. Yan, J. H. Lin, D. Kennedy, and F. W. Williams, "Random vibration analysis for coupled vehicle-track systems with uncertain parameters," *Engineering Computations*, vol. 33, no. 2, pp. 443–464, 2016.

[21] X. F. Zhang, X. K. Wang, M. D. Pandey, and J. D. Sørensen, "An effective approach for high-dimensional reliability analysis of train-bridge vibration systems via the fractional moment," *Mechanical Systems and Signal Processing*, vol. 151, Article ID 107344, 2021.

[22] W. Guo, C. Zeng, H. Y. Gou et al., "Real-time hybrid simulation of high-speed train-track-bridge interactions using the moving load convolution integral method," *Engineering Structures*, vol. 228, Article ID 111537, 2021.

[23] H. L. Li, T. Y. Wang, and G. Wu, "A Bayesian deep learning approach for random vibration analysis of bridges subjected to vehicle dynamic interaction," *Mechanical Systems and Signal Processing*, vol. 170, Article ID 108799, 2022.

[24] X. Zhang, Y. Han, L. D. Wang, H. Y. Liu, and C. S. Cai, "An adaptive surrogate model approach for random vibration analysis of the train–bridge system," *Engineering Structures*, vol. 278, Article ID 115490, 2023.

[25] Z. H. Zhai, C. B. Cai, and S. Y. Zhu, "Implementation of Timoshenko curved beam into train-track-bridge dynamics modelling," *International Journal of Mechanical Sciences*, vol. 247, Article ID 108158, 2023.

[26] H. Xia and N. Zhang, "Coupling vibration of train-bridge system," China Science Publishing & Media Ltd, Beijing, China, 2014.